The Influence of Additives on Sintering and Microstructural Evolution of SiC

Eran Gros

The Influence of Additives on Sintering and Microstructural Evolution of SiC

Research Thesis

In Partial Fulfillment of the

Requirements for the Degree of

Master of Science in Material Science and Engineering

Eran Gros

Submitted to the Senate of

the Technion – Israel Institute of Technology

The research thesis was done under the supervision of Prof. W.D. Kaplan in the Department of Materials Science and Engineering.

Acknowledgements

I would like to express a deep gratitude to my supervisor Prof. Wayne D. Kaplan for his inspiration and constant encouragement. For teaching me how to conduct a research and introduced me to the world of ceramics. I also appreciate the fruitful discussions around the clock

Table of contents

1 Introduction 1
2 Literature Survey 3
2.1 SiC Properties 3
2.2 Ceramic Processing 5
2.2.1 Powder Processing 5
2.2.2 Sintering 5
2.2.3 Pressureless Sintering of SiC 8
2.2.4 Sintering Conditions 9
3 Research Goals 10
4 Experimental Methods 11
4.1 Processing SiC 11
4.1.1 Powder Processing 11
4.1.2 Green Body Formation 12
4.1.3 Sintering 14
4.2 Model Experiment 14
4.2.1 Sample Preparation 14
4.2.2 Oxidation 15
4.2.3 Coating 15
4.2.4 Reduction 15
4.3 Characterization Methods 16
4.3.1 Sample Preparation 16
4.3.2 Scanning Electron Microscopy 16
4.3.3 Transmission Electron Microscopy 17
4.3.4 Density Measurements 17
4.3.5 Grain Size Measurements 17
5 Results 19
5.1 Sintering Process 19
5.1.1 Green Body and Powder Processing 19
5.1.2 Sintering Experiments 22
5.2 Reduction Experiments 30
6 Discussion 36
6.1 Sintering Process 36

6.1.1 The Influence of Powder Processing on the Green Body 36
6.1.2 The Influence of Compaction Method on the Green Body Density 37
6.1.3 The Influence of Sintering Temperature and Time 39
6.1.4 The Influence of Sintering Additives on the Microstructure 40
6.2 Reduction Experiments 42
6.3 SiO_2 Densification Inhibition Mechanism 44
7 Summary and Conclusions 46
8 Recommendation for Future Work 47
9 References 48

List of Figures

Figure 1: Polymorphs and polytypes of SiC, marked as xH/xR/xC where x represents the number of (0001) or (001) planes in the unit cell, H/R/C stands for hexagonal, rhombohedral or cubic, respectively. 3
Figure 2: Illustration: the reduction of total surface energy during sintering by coarsening and densification. 6
Figure 3: Different matter transfer paths during sintering for a two spheres model. Ds is the surface diffusion coefficient; D_{gb} is the grain boundary diffusion coefficient; Dl the lattice diffusion coefficient; η viscosity for viscous flow; and Δp the pressure gradient for evaporation-condensation process. 8
Figure 4 Uniaxial pressing scheme, the powder was pressed using a manual hydraulic uniaxial press at 27 MPa in 3 load cycles for each sample. 13
Figure 5: Cold isostatic pressing (CIP) scheme. The samples were pressed at 240 MPa isostatic pressure. 14
Figure 6: SE SEM micrographs of the as-received powder. a) Low magnification of agglomerates on a carbon adhesive tape, b) high magnification image of one of the agglomerates showing the individual powder grains. 19
Figure 7: Photographs of green bodies that were pressed using: a) uniaxial pressing at 27 MPa without the use of sintering additives or binder. The green body crumbled while being extracted out of the mold. b) Uniaxial pressing at 27 MPa with sintering additives and binder; c) uniaxial pressing at 27 MPa with sintering additives and binder followed by CIP at 240 MPa; d) CIP at 240 MPa without sintering additives or binder. 20
Figure 8: SE SEM micrographs of a green body pressed using uniaxial pressing at 27 MPa followed by CIP at 240 MPa, with the addition of a binder, reaching a green density of ~65%. The sample was fired at 1700°C for 30 minutes in flowing He. 21
Figure 9: Comparison of the green density for each pressing method. 21
Figure 10: SE SEM micrographs, showing the fracture surface of SiC samples sintered at 2100°C for 30 min without the use of sintering additives after pressing by CIP: a) without powder processing; b) after powder processing. 22
Figure 11: SE SEM micrographs of the fracture surface of SiC sintered without sintering additives, showing a coarse porous microstructure of interconnected grains of various sizes.

a) Sintered at 1700°C for 30 min; b) sintered at 1900°C for 30 min; c) Sintered at 2100°C for 30 min; and d) Sintered at 2100°C for 3 hours. 23
Figure 12: BF TEM diffraction contrast micrograph of a SiC sample sintered at 2100°C for 30min without the use of sintering additives. An amorphous SiO_2 phase (red arrow) was identified using EDS. a) Crystalline SiC grains with amorphous SiO_2 phase. The electron diffraction pattern of the arrowed (yellow arrow) grain shows the $[2\bar{4}23]$ zone axis of SiC 6H (shown in the inset). b) High magnification micrograph of the amorphous phase in a)..... 24
Figure 13: EDS spectrum of the arrowed area in Figure 12 showing the presence of SiO_2. 25
Figure 14: SE SEM micrographs (fracture surface) of SiC sintered at 2100°C for 1 hour with 3 wt.% carbon (6% phenolic resin) and a) 0.5 wt.% B, b) 1 wt.% B..... 26
Figure 15: SE SEM micrographs (polished and thermally etched) of SiC doped with 0.5 wt.% B and 6 wt.% C for 4 hours at various temperatures: a-b) 1950°C; c) 2050°C; d) 2100°C. 27
Figure 16: Grain size measurement for SiC samples sintered at 2100°C for different times, doped with 0.5 wt.% B and 3 wt.% C. 28
Figure 17: Density measurements for SiC samples doped with 0.5 wt.% B and 3 wt.% C at different sintering temperatures and time. 28
Figure 18: SE SEM micrographs (fracture surface) of SiC sintered at 2100°C for 1hr, doped with 0.5 wt.% B. 29
Figure 19: SE SEM micrographs (fracture surface) of SiC sintered at 2100°C for 1hr, doped with 3 wt.% C, showing porous microstructure and flake like features (arrowed) on the surface of the grains. 30
Figure 20: BF diffraction contrast TEM micrographs of SiC sintered at 2100°C for 1hr, doped with 3 wt.% C. The arrowed areas are amorphous phases (determined using electron diffraction) of varying compositions of $Si_xO_yC_z$, Si_xO_y, and Si. 30
Figure 21: HRTEM micrographs of a plan-view sample of single crystal SiC in the [0001] orientation, (a) immediately after preparation, showing a ~2nm thick amorphous layer due to ion milling; (b) after oxidation at 1400°C, showing ~30 nm amorphous layer, the transition from amorphous to crystalline can be seen using the FFT analysis (shown on the micrograph); and by (c) high magnification of the transition area. (d) After carbon coating and reduction at 1400°C, showing a ~1nm thick amorphous layer. 32

Figure 22: HRTEM micrograph of a cross-section oxidized (at 1100°C) SiC single crystal wafer in a [$\bar{1}2\bar{1}0$] zone axis, showing ~17nm thick amorphous layer on the surface of the wafer. 33
Figure 23: EDS analysis of the amorphous layer, shown in Figure 22..... 33
Figure 24: Micrographs of a reduced (at 1400°C) plan-view sample: a) SE SEM micrograph; b) BF TEM micrograph. Both micrographs show the same region of the sample (mirror inversion). The edge of the sample is partially covered with a thick SiO_2 layer. Ni contaminants are also present on the surface. 34
Figure 25: SE SEM micrographs of a reduced (1400°C) SiC single crystal wafer showing: a) the circular crater-like feature; b) high magnification of the outer region (arrowed); and c) high magnification of the inner region (arrowed). 35
Figure 26: Schematic illustration of the microstructure of an individual agglomerate containing intra-agglomerate pores, and the microstructure of the green body formed from an agglomerated powder, containing inter-agglomerate pores..... 37
Figure 27: Illustration of the density profile inside a uniaxially pressed green body (redrawn from [22]). 38
Figure 28: Grain size distribution and a log-normal fitting curve analysis for a SiC sample doped with carbon and boron, sintered at 2100°C for 4 hours. 40
Figure 29: Oxide layer profile caused by the formation of a cristobalite precipitate [29]..... 44
Figure 30: The surface energies in the SiC/SiO_2 system. 45

List of Tables

Table 1: A summary of the common polytypes in SiC with their corresponding lattice parameters and theoretical density [3]. 4
Table 2: SiC 6H powder (0.7μm, Electro abrasives LLC) used in this study. 11
Table 3: List of the sintering additives used and the role of each additive. 12
Table 4: Density measurements of samples sintered without sintering additives at different temperatures and times. 24
Table 5: Density measurements for sample sintered at 2100°C with 3 wt.% C 26

Abstract

A pressureless solid phase sintering process for silicon carbide (α-SiC 6H) was developed and optimized using boron and carbon as sintering additives. The as-received powder was ball-milled with the sintering additives and a deflocculant. After drying and sieving, the powder was compacted using uniaxial pressing followed by cold isostatic pressing. The green bodies were sintered in a carbon resistance furnace under flowing He at 2100°C. The influence of the sintering additives and sintering conditions on the density and microstructure were evaluated using scanning electron microscopy, transmission electron microscopy and density measurements. Undoped samples did not sinter, and the microstructure was characterized by particle coarsening and a film of SiO_2. Samples sintered with only boron or carbon did not sinter. The carbon-doped samples had a microstructure which was similar to the undoped samples; containing coarsened particles, a porous microstructure, and an amorphous film containing silicon, carbon and oxygen. Samples doped with 0.5 wt.% boron and 3 wt.% carbon sintered to a density of 96% with a microstructure of mostly uniaxial grains.

The role of carbon in reducing SiO_2 during solid-state sintering of SiC was directly shown using a model experiment, where transmission electron microscopy was used to follow oxidation and reduction of the surface of SiC single crystal. The lack of densification for undoped samples is explained by the low surface energy of SiO_2 compared to the grain boundary energy of SiC, which reduces the driving force for densification

List of Symbols and Acronyms

T_m	Melting Temperature
γ	Surface/interface energy of a particle
A	Total surface
r_1, r_2	The radii of curvature perpendicular with each other at the interface
k	Curvature
T	Temperature
P	Pressure
t	Time
SEM	Scanning electron microscope
TEM	Transmission Electron Microscope
HRTEM	High Resolution Transmission Electron Microscopy
STEM	Scanning Transmission Electron Microscope
EDS	Energy Dispersion Spectroscopy
pH	Power of hydrogen
Pa	Pascal
°C	Celsius
ρ	Density
SAD	Selected Area Diffraction
wt.%	Weight percent
P	Pressure
MPa	Mega pascal
SE	Secondary electrons
BF	Bright field
s.e	Standard error
s	Standard deviation
N	Number of measurements
γ_{SV}	Solid-vapor surface energy
γ_{LV}	Liquid-Vapor surface energy
γ_{GB}	Grain-boundary surface energy

1 Introduction

Silicon carbide is a ceramic material used in numerous applications such as automobile brake-pads, ball bearings, ballistic body armor and other applications requiring good wear and temperature resistance [1]. SiC is also used in the semiconductor industry as a wide band-gap semiconductor with a high-temperature resistance. For most of its structural applications, SiC is used in a polycrystalline form. Sintering of SiC is done at temperatures above 2000°C using either pressure assisted or pressureless sintering, and by either liquid state sintering with the addition of secondary phases such as Al_2O_3 and Y_2O_3, or by solid state sintering [2]. The selected sintering method affects both the mechanical and functional properties of SiC, which strongly depends on the microstructure and the presence of secondary phases [3].

Pressureless solid state sintering of SiC is the preferred sintering method for both economic reasons and in order to avoid the presence of secondary phases that may affect the mechanical properties; it is known to require the use of sintering additives, mostly boron and carbon [4]. The roles of both boron and carbon were investigated in several previous works; the role of carbon is thought to be the reduction of surface SiO_2, which due to an unknown mechanism inhibits mass transfer mechanisms that promote densification. The role of boron is unknown and is thought to be the inhibition of surface diffusion or the promotion of grain boundary diffusion that is required for densification. However, as most works address indirect microstructural parameters such as pore size and volume, a direct approach for showing any of these proposed roles was never attempted. In order to understand the role for either one of the additives, a model experiment is required, which truly isolates the sintering process parameter.

Without the use of additives for pressureless sintering of SiC, a coarse and porous vermicular microstructure is formed, with virtually no densification. This phenomenon was also studied in previous works, and was explained as resulting from some intrinsic properties of the material, such as the covalent nature of the Si-C bonds, or as due to a high grain boundary energy that suppresses densification.

In order to fully understand the formation of the porous microstructure and the sintering characteristics of SiC it is critical to address thermodynamics considerations that are involved in the sintering process, in terms of surface and grain boundary energies, and by considering all the surfaces and interfaces in the system.

The primary goal of this research is to achieve a better understanding on the sintering physics of SiC by studying the influence of the sintering additives, temperature and time on the microstructural evolution. This goal was achieved by developing a pressureless solid state sintering process for SiC, which was characterized using scanning electron microscopy (SEM), transmission electron microscopy (TEM), energy dispersive spectroscopy (EDS), and density measurements. Moreover, using a model experiment, the role of carbon as reducing agent for surface SiO_2 was directly shown.

2 Literature Survey

2.1 SiC Properties

Two main polymorphs exist in SiC [5]: a cubic polymorph of a Zinc-blend structure, named β-SiC and a hexagonal polymorph of a Wurtzite structure named α-SiC, with over 250 different polytypes. The polytypes in SiC are a one-dimensional ordering sequence of SiC_4 (or CSi_4) layers of tetrahedra, linked through their vertices, without any variation in stoichiometry, along the [0001] axis of the unit cell as shown in Figure 1. The polytypic stacking is defined, using one of several methods to define the sequence [6], by the number of SiC_4 layers present in the unit cell. For example, the 15R polytype represents 15 layers of SiC_4 layers stacked in a rhombohedral unit cell. The most common polytypes/polymorphs of SiC are 3C, 4H, 6H and 15R [3]. Table 1 summarize the crystallographic parameters and density of some of the most common SiC polytypes.

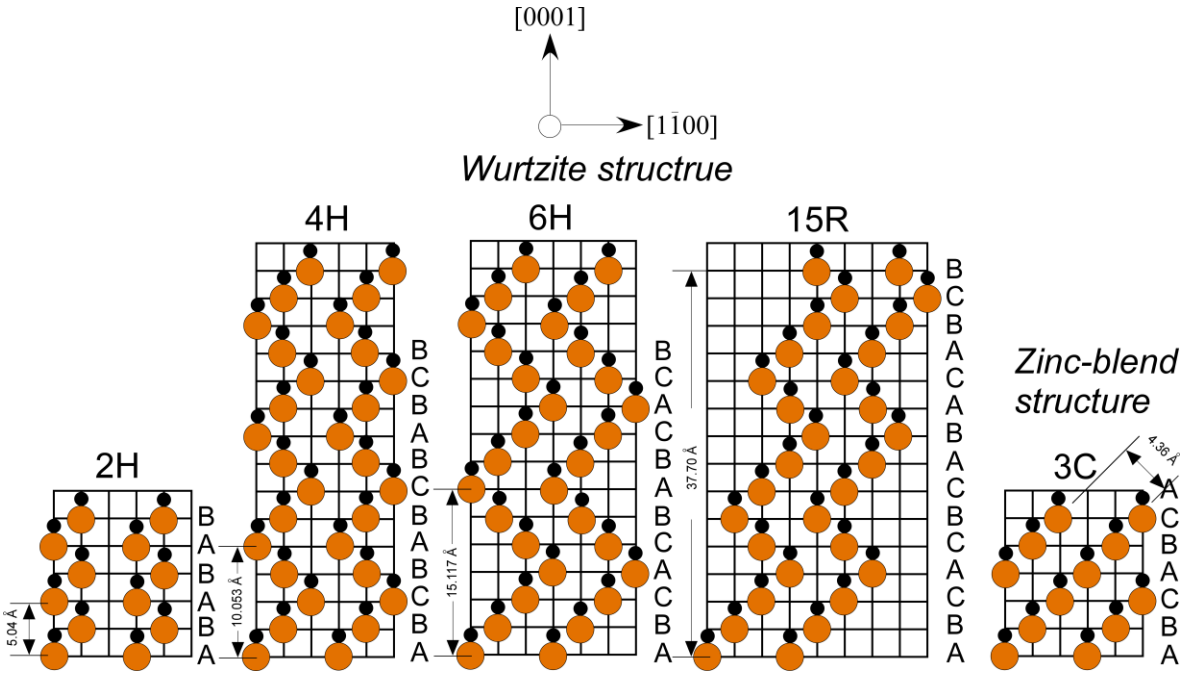

Figure 1: Polymorphs and polytypes of SiC, marked as xH/xR/xC where x represents the number of (0001) or (001) planes in the unit cell, H/R/C stands for hexagonal, rhombohedral or cubic, respectively.

Table 1: A summary of the common polytypes in SiC with their corresponding lattice parameters and theoretical density [3].

Polytype	**Lattice parameter (nm)**	**Density (g/cm^3)**
2H	a=0.3081, c=0.5031	3.219
3C	a=0.43589	3.215
4H	a=0.3081, c=1.0061	
6H	a=0.3081, c=1.5092	
15R	a=0.3073, c=3.770	
21R	a=0.3073, c=5.278	

SiC is considered as one of the hardest known materials with a typical Vickers hardness in the range of 2500-2700 for solid state sintered SiC with boron and carbon as additives. The fracture toughness of SiC, as measured using the CNB method is 3.2 MPa·m$^{0.5}$ and varies as a function of grain size, doping and preparation method of the specimen [3].

SiC is used for a variety of applications, such as ballistic armor, novel automobile systems, and other applications requiring high temperature and good wear resistance. SiC is also a wide band gap semiconductor with many industrial applications such as high frequency and high-temperature CPUs and LEDs.

2.2 Ceramic Processing

2.2.1 Powder Processing

In order to produce a dense ceramic material, several processing steps are required, starting with processing of the powder. In order to break powder agglomerates that may decrease the density of the green body, the powder is mixed in a fluid medium with a dispersant (deflocculant) which results in a dispersed suspension also known as a slip. The role of the deflocculant is important because sub-micron particles have a high specific surface area, which promote flocculation and particle agglomeration in the liquid phase, where flocs are held together by long range Van der Waals forces [7]. Deflocculants can increase/decrease the pH of the slip to be significantly different from that of the isoelectric point of the particle, resulting in breaking of soft agglomerates. The deflocculant may also reduce the effective surface tension of the powder particles, thus decreasing the inter-particle attraction forces. Ball-milling is used for mechanically breaking the agglomerates together with the dispersive effect of the deflocculant. After deflocculation, the slip is dried, sieved and pressed to a green body which is then sintered at elevated temperatures.

2.2.2 Sintering

Sintering is the process of densification and consolidation of a powder compact, typically in the range $0.5\ T_m<T<0.8\ T_m$. The thermodynamic driving force for sintering is the reduction of the total surface energy of the system following equation (1)

$$\Delta(\gamma A)= \Delta\gamma A+ \Delta A\gamma \qquad (1)$$

where γ is the specific surface/interface energy and A is the total surface/interface area of the system [8]. The term γA is the total surface energy of the powder compact, which as illustrated in Figure 2, can be lowered in two ways,

1. **Densification**: Reduction of the average surface/interface energy (**Δγ**) by replacing the high energy surfaces in the green body with (lower energy) grain boundaries.
2. **Coarsening:** Reduction of the total surface area of the system (**ΔA**) by the growth of large grains with a low specific surface/interface area, at the expense of smaller grains of high specific surface/interface area.

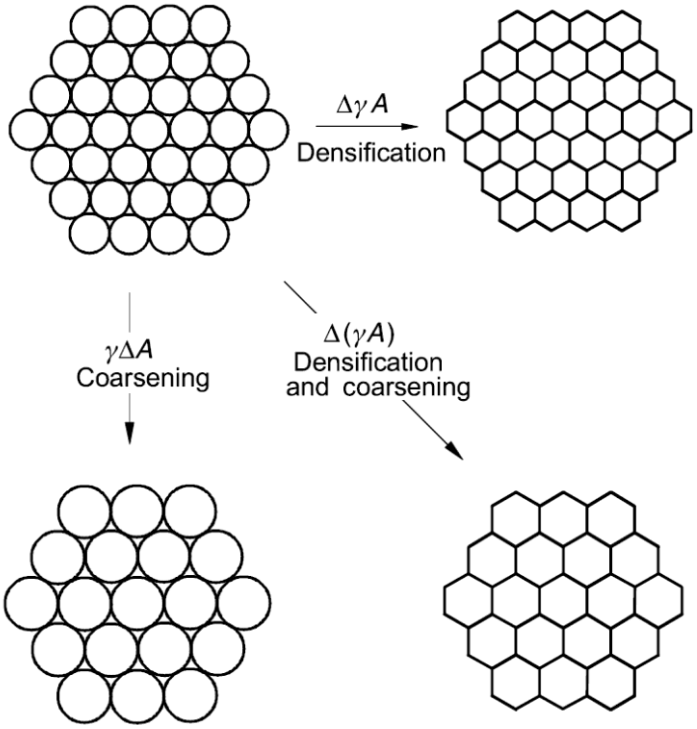

Figure 2: Illustration: the reduction of total surface energy during sintering by coarsening and densification.

Densification and coarsening are competitive processes which can take place simultaneously, as both are driven by the local pressure gradients due to the surface curvature of the system, defined as:

$$k = \left(\frac{1}{r_1} + \frac{1}{r_2} \right) \tag{2}$$

where, r_1 and r_2 are the perpendicular radii of curvature at the interface. The sign of the curvature is chosen to be positive for convex surfaces and negative for concave surfaces. The

pressure gradient across a curved interface of curvature k, driven from the Gibbs equation for the free energy of the interface, is given by the Young-Laplace equation:

$$P^{\alpha} - P^{\beta} = \Delta P = \gamma\left(\frac{1}{r_1} + \frac{1}{r_2}\right) = \gamma k \tag{3}$$

Matter is therefore transferred during solid state sintering, by the migration of atoms from convex to concave regions, or the migration of vacancies in the opposite direction.

The two main types of sintering mechanisms are solid state sintering and liquid state sintering. During solid state sintering, diffusion takes place in the bulk, grain boundaries, and the surface of the grains. During liquid state sintering a secondary molten liquid phase is present between the solid grains, allowing for an additional diffusion path through the liquid, and induces capillary forces that promote densification.

As illustrated in Figure 3, matter can be transferred during solid phase sintering by the following mechanisms:

1. Bulk diffusion (D_b: bulk diffusion coefficient);
2. Grain boundary diffusion (D_{GB}: grain boundary diffusion coefficient);
3. Surface diffusion (D_s: surface diffusion coefficient);
4. Vapor phase diffusion (ΔP: pressure gradient);
5. Viscous flow (η; viscosity).

These mechanisms determine the sintering kinetics which control the rates at which coarsening and densification occur. Full densification is achieved by bulk diffusion, grain boundary diffusion and viscous flow, which allows for vacancy diffusion through the bulk and is necessary for the elimination of closed pores. Vapor and surface diffusion contribute

mostly to coarsening as these mechanisms can transfer matter only to the point where the pores are open (interconnected).

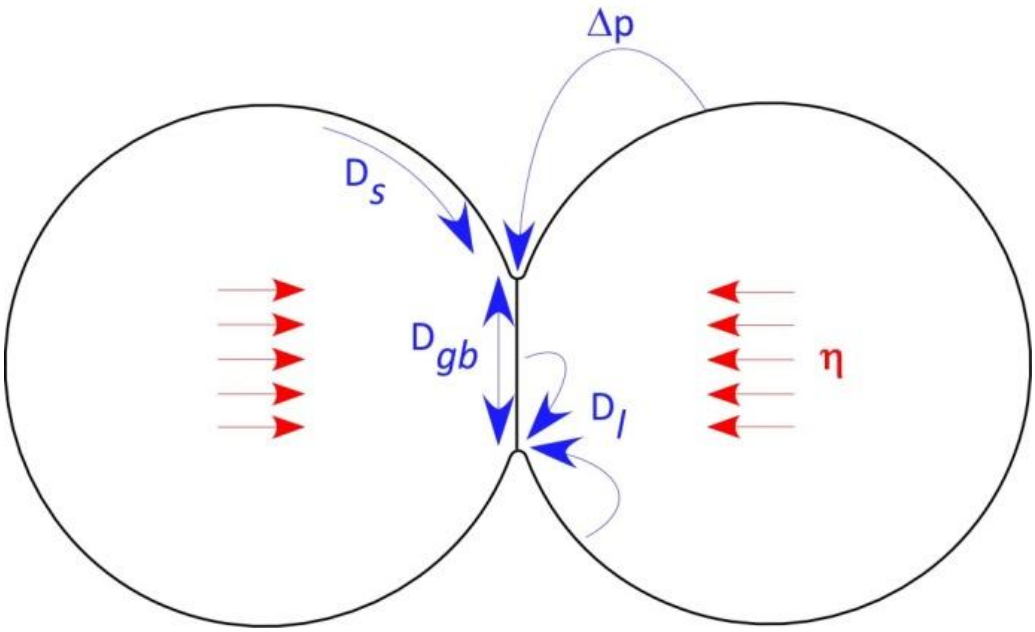

Figure 3: Different matter transfer paths during sintering for a two spheres model. Ds is the surface diffusion coefficient; D_{gb} is the grain boundary diffusion coefficient; Dl the lattice diffusion coefficient; η viscosity for viscous flow; and Δp the pressure gradient for evaporation-condensation process.

2.2.3 Pressureless Sintering of SiC

There are two main approaches for pressureless sintering of SiC: solid-state sintering and liquid state sintering, which differ in the resulting mechanical properties [3,9]. For solid-state sintering, SiC is usually the dominant phase, resulting in improved mechanical properties compared to SiC processed by liquid state sintering which usually includes significant amounts of secondary phases [10]. Solid-state sintering of SiC is performed mainly by using boron and carbon as sintering additives [4,11]; without the use of both carbon and boron, a porous vermicular microstructure will form with very little densification [4,12].

The roles of boron and carbon in the solid state sintering of SiC were studied in several past works [12,13,14,15]. The role of boron was suggested to be either the inhibition of surface

diffusion and evaporation-condensation or an increase of bulk or grain-boundary diffusion rates [12,13]. The role of carbon was suggested to be the reduction of surface SiO_2 that inhibits the densification process via a mechanism of unknown nature, following the reaction [12,13,15]:

$$\mathbf{SiO_2+3C=SiC+2CO} \quad (4)$$

This reaction reaches a maximum rate at 1400°C [15]. It is worth noting that while SiO_2 is in a liquid state at the elevated temperatures commonly used for sintering SiC (~2100°C), liquid-state sintering will not occur for oxidized SiC powders even though SiO_2 can be used for liquid state sintering of SiC [16]. The actual mechanism(s) by which both these additives (boron and carbon) promote solid-state sintering are still under debate.

2.2.4 Sintering Conditions

Pressureless solid state sintering of SiC requires a low $P(O_2)$ atmosphere since SiC, boron and carbon react with oxygen at elevated temperatures, with equilibrium $P(O_2)$ as low as 10^{-15} atm for boron. Flowing He is often used, providing both a low oxygen content and high permeability of the He atoms through the sample. The sintering temperatures required for reaching high density are in the range of 2020°C to 2100°C [13]. For temperatures lower than 2000°C, only little densification is achieved [17].

3 Research Goals

The goals of this research were first to develop and optimize the manufacturing process of SiC by pressureless solid state sintering, using boron and carbon as sintering additives, for a better understanding on the influence of the sintering additives on the microstructural evolution during the sintering. A secondary goal was to elucidate the role of carbon as a reducing agent of surface SiO_2 in the sintering process using a model experiment.

4 Experimental Methods

4.1 Processing SiC

4.1.1 Powder Processing

SiC 6H powder (0.7μm, Electro abrasives LLC, specification are listed in Table 2) was used for the sintering processes. The powder was ball milled using a 5 mm SiC balls, in acetone at volume ratio of 1:1, and deflocculant (KV 9056, Zschimmer & Schwarz) inside a polyethylene tube for 12 hours. During the ball milling process, the powder was mixed together with the sintering additive listed in Table 3.

Table 2: SiC 6H powder (0.7μm, Electro abrasives LLC) used in this study.

Typical chemical analysis		**Typical particle sizing (Horiba)**	
SiC	98.5 wt.% min.	**D90**	1.811 μm
Free C	2 wt.% max.	**D50**	0.748 μm
O	1.1 wt.% max.	**D10**	0.344 μm
N	0.25 wt.% max.		
Si	0.63 et.% max.		
Fe	800 ppm max./ 300 ppm typical		
Ca	200 ppm max./ 10 ppm typical		
Mo	200 ppm max./ 50 ppm typical		
Al	550 ppm max./ 150 ppm typical		
Zr	50 ppm max./ 12 ppm typical		

Table 3: List of the sintering additives used and the role of each additive.

Additive	Role	Quantity
Boron (amorphous boron, Sigma-Aldrich)	Boron addition	0.5-1 wt.%
Carbon Black	Carbon addition and lubricant	0.5 wt.%
Phenolic resin (Para-butyl-tertio-phenol formaldehyde resin; Ribetak 7522E, SI Group Inc)	Carbon addition and Binder	6 wt.%

After ball milling, the powder was dried in a low-temperature air furnace at 60°C for 6 hrs. The dried powder was then manually ground using a mortar and pestle, and sieved through a set of decreasing sieve sizes (96, 72, 50, 25 μm).

4.1.2 Green Body Formation

Uniaxial pressing and cold isostatic pressing (CIP) were used as pressing methods. Uniaxial pressing was done using a 2 cm and 3 cm in diameter cylindrical molds made of two steel pistons inside a steel cylinder with a Teflon lining to reduce friction, as shown schematically in Figure 4.

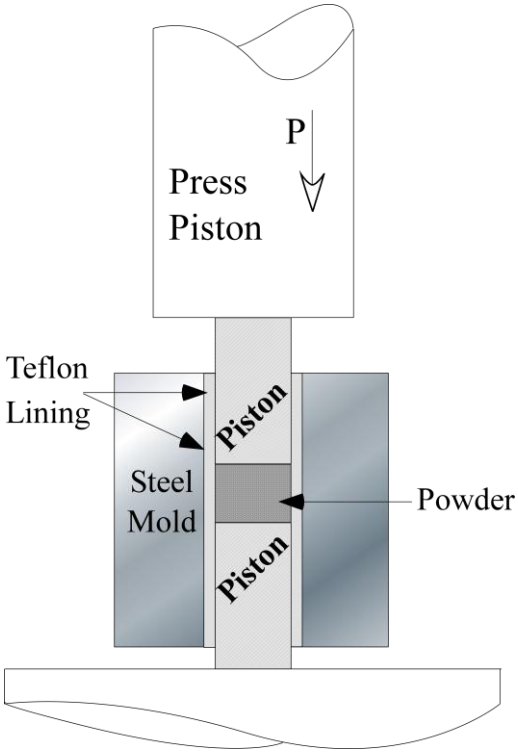

Figure 4 Uniaxial pressing scheme, the powder was pressed using a manual hydraulic uniaxial press at 27 MPa in 3 load cycles for each sample.

CIP was done using a pressure vessel filled with pressurized oil (glycerol) at 240 MPa as described schematically in Figure 5. The samples were sealed in vacuum (rubber) bags to prevent contact with the oil and to avoid residual stresses in the green body due to pressurized trapped air.

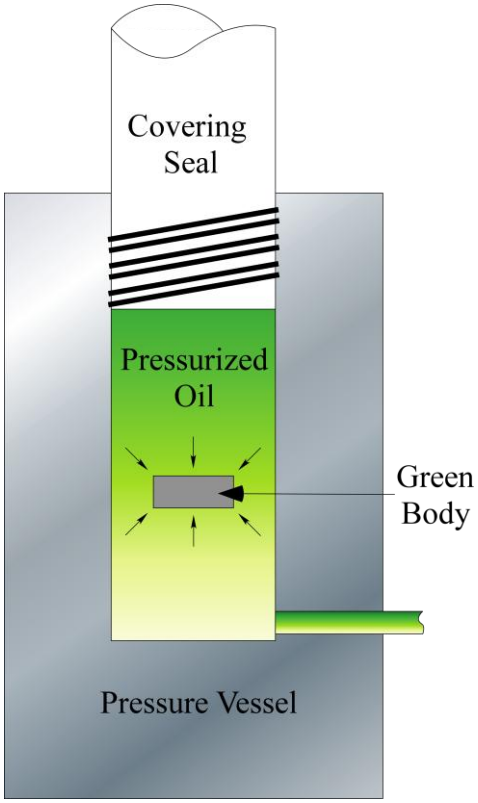

Figure 5: Cold isostatic pressing (CIP) scheme. The samples were pressed at 240 MPa isostatic pressure.

4.1.3 Sintering

Sintering was done using a high-temperature resistance furnace (Thermal Technology Inc, Model 1000) with graphite heating elements and crucibles under flowing He (99.995%) to obtain a low oxygen partial pressure, using heating and cooling rates of 15°C/min. The temperature was controlled and measured using a thermocouple for temperatures lower than 2000°C and an optical pyrometer for the higher temperatures.

4.2 Model Experiment

4.2.1 Sample Preparation

Transmission electron microscopy (TEM) plan-view samples were prepared for a sequence of oxidation-reduction processes as a model experiment for the role of carbon in the reduction of surface SiO_2 from SiC during sintering. Cross-section samples were prepared using the

method described in section 4.3.1 using SiC 6H (0001) single crystal wafers (Xiamen Powerway Advanced Material, N-doped). Additional samples for plan-view analysis were prepared from the same single crystal wafers, which were sliced into 2x2 cm squares.

4.2.2 Oxidation

In order to simulate a native oxide layer on the surface of the SiC powder grains, the SiC single crystals were thermally oxidized. Oxidation was done using a resistance furnace in air, at a heating rate of 15°C/min to 1400°C or 1100°C with no dwelling time, and a cooling rate of 15°C/min.

4.2.3 Coating

In order to simulate the addition of carbon to the SiC powder during sintering, the oxidized single crystal samples were coated with a ~10nm thick carbon layer using a carbon coater (Q150T Turbo-Pumped Carbon Coater, Quorum Technologies).

4.2.4 Reduction

The reduction of the SiO_2 from the surface of the single crystal SiC samples was done using the same furnace used to sinter the bulk powder samples (see section 4.1.3). The samples were heated at a heating rate of 15°C/min to 1400°C with no dwelling time, and cooled at a rate of 15°C/min. The temperature was selected to fit the maximum reduction rate of SiO_2 [15].

4.3 Characterization Methods

4.3.1 Sample Preparation

For grain size and morphology characterization, samples were polished using diamond polishing suspensions with polishing cloths, and a final polish using a colloidal silica suspension. The polished samples were thermally etched at 1700°C for 30 minutes [18]. All of the polished SEM samples were coated with carbon to prevent charging under the electron beam.

For TEM characterization, plan view samples were prepared by grinding and polishing 3 mm diameter discs to a thickness of ~100 μm. The discs were dimpled using a dimpling grinder (Fischione model 150) to a thickness of 15 μm, and thinned to perforation using an Ar ion miller (Gatan PIPS), followed by low energy Ar ion polishing (Technoorg LINDA Gentle mill) for the removal of residual amorphous damage due to the milling process.

Cross-section samples were made from single crystal wafer slices that were glued together using a thermosetting epoxy resin, then mechanically polished using a 5μm diamond lapping tape, followed by Ar ion milling (Gatan PIPS) for final thinning.

4.3.2 Scanning Electron Microscopy

Scanning electron microscopy (SEM) was done using an FEI E-SEM Quanta 200 and a Zeiss Ultra-Plus FEG-SEM. Energy dispersive spectroscopy (EDS) mounted on the SEMs was used to confirm the various phases in the samples.

4.3.3 Transmission Electron Microscopy

Conventional TEM was conducted at 200 kV, using an FEI Tecnai G^2 T20 S-Twin TEM. High-resolution TEM (HRTEM) was conducted at 300 kV using a monochromated and (image) aberration corrected FEI Titan 80-300 KV S/TEM. EDS mounted on the TEMs was used to confirm the various phases in the samples

4.3.4 Density Measurements

The density of the sintered specimens was measured using the Archimedes method following ASTM standard C830 calculated using:

$$\rho_{specimen} = \frac{D}{W - S} \cdot \frac{1}{\rho_{SiC}} \tag{5}$$

where *D* is the weight of the dry specimen, W is the saturated weight, S is the suspended (in water) weight and ρ_{SiC} is the theoretical density of SiC, which is 3.21 gr/cm^3. Each sample was sliced into 6 non-identical pieces; the average of the measurements was taken as the nominal density and the standard deviation as the measurement error.

4.3.5 Grain Size Measurements

Grain size analysis was done based on SEM micrographs using the linear intercept method from about 200 grains form each sample [19]. A correction factor of 1.57 was used to correlate between the average grain size $\bar{G}$ and the average intercept length $\bar{L}$ so that:

$$\bar{G} = 1.56\bar{L} \tag{6}$$

The standard error was taken as the standard error of the mean:

$$s.e = \frac{s}{\sqrt{N}} \tag{7}$$

where s is the standard deviation of the sample and N is the total number of measurements.

5 Results

5.1 Sintering Process

5.1.1 Green Body and Powder Processing

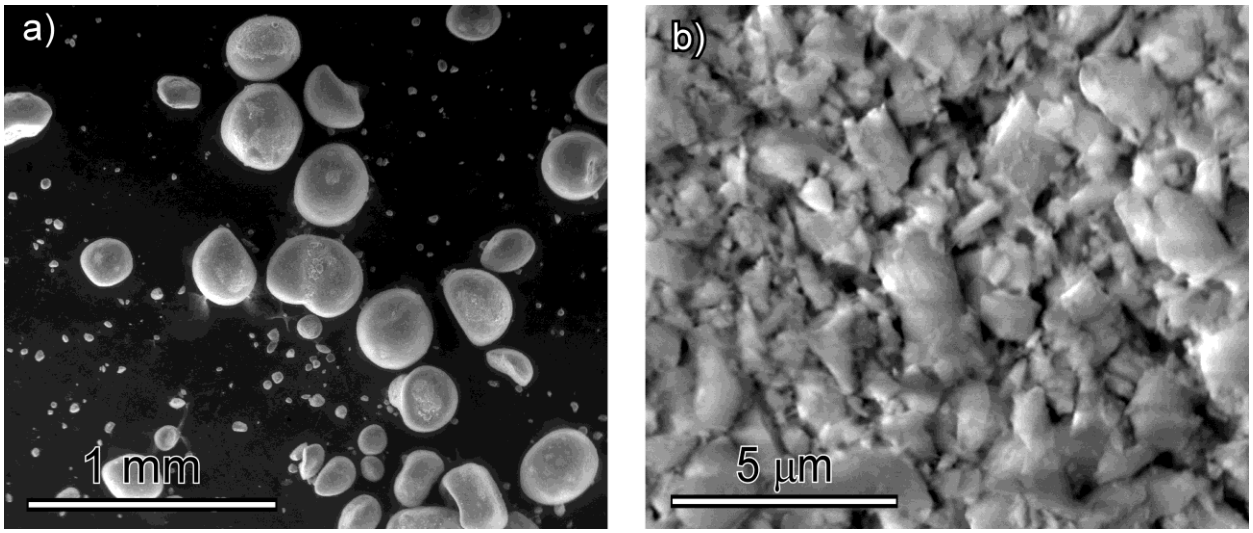

Figure 6: SE SEM micrographs of the as-received powder. a) Low magnification of agglomerates on a carbon adhesive tape, b) high magnification image of one of the agglomerates showing the individual powder grains.

The processed powder was pressed to a green body using uniaxial pressing and CIP. The influence of the pressing method, as well as the addition of binder and lubricant on the density and structural integrity, were evaluated. Figure 7a shows a photograph of a uniaxially pressed green body from SiC powder, processed without a binder or lubricant that broke while being extracted from the pressing mold. Figure 7b shows a photograph of a uniaxially pressed (27 MPa) green body, from a SiC powder processed with both binder (6 wt.% phenolic resin) and lubricant (0.5 wt.% carbon black), showing a few cracks across the sample after applying a little force (by hand). Figure 7c displays a green body uniaxially pressed at 27 MPa followed by CIP at 240 MPa, with both binder and lubricant. Figure 7d presents a green body pressed using CIP with no binder or lubricant.

Figure 8 presents a SEM micrograph of a green body fired at 1700°C, pressed by uniaxial pressing followed by CIP. The shape and size distribution of the SiC grains can be seen, as well as the close packing of the green body due to the improved pressing method.

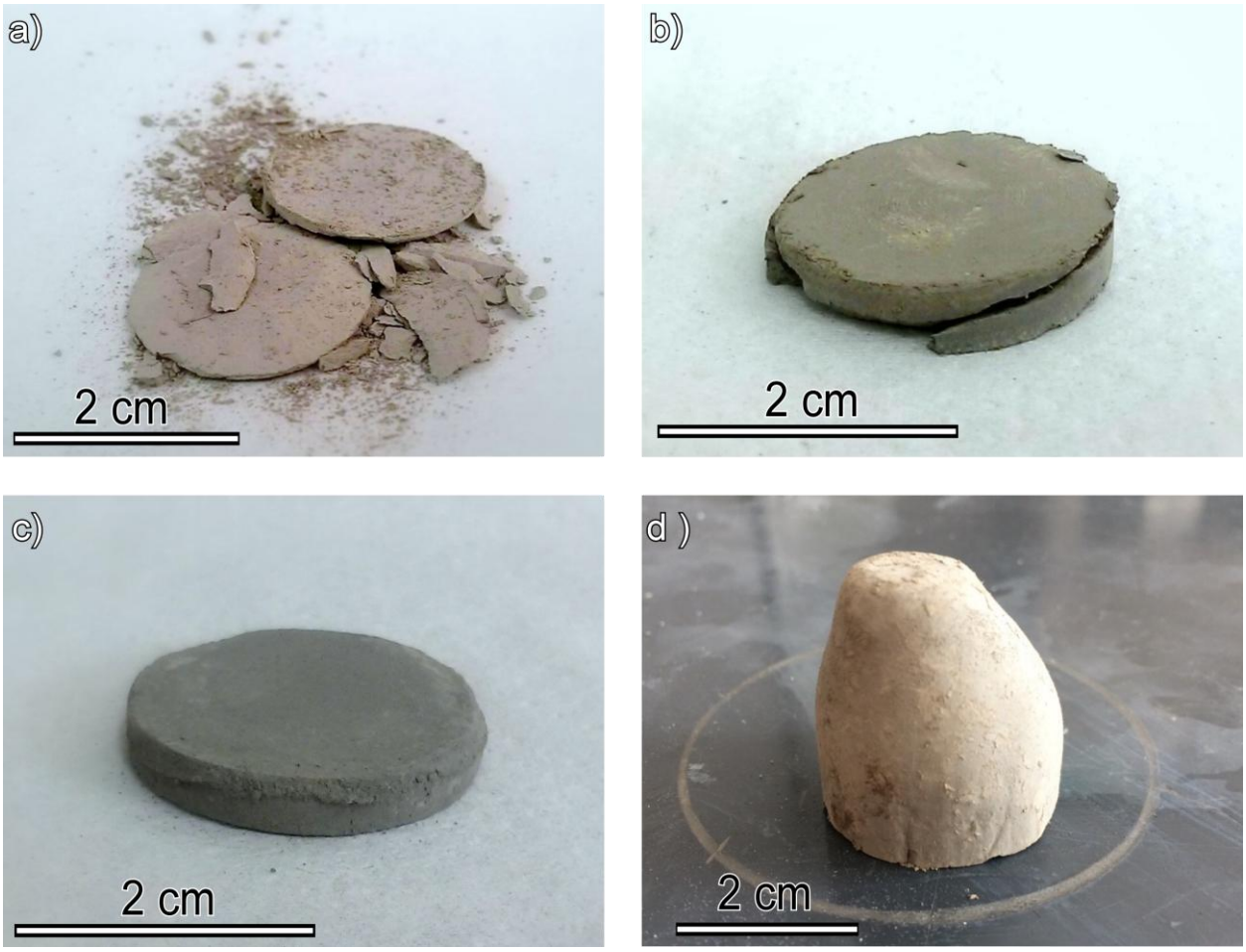

Figure 7: Photographs of green bodies that were pressed using: a) uniaxial pressing at 27 MPa without the use of sintering additives or binder. The green body crumbled while being extracted out of the mold. b) Uniaxial pressing at 27 MPa with sintering additives and binder; c) uniaxial pressing at 27 MPa with sintering additives and binder followed by CIP at 240 MPa; d) CIP at 240 MPa without sintering additives or binder.

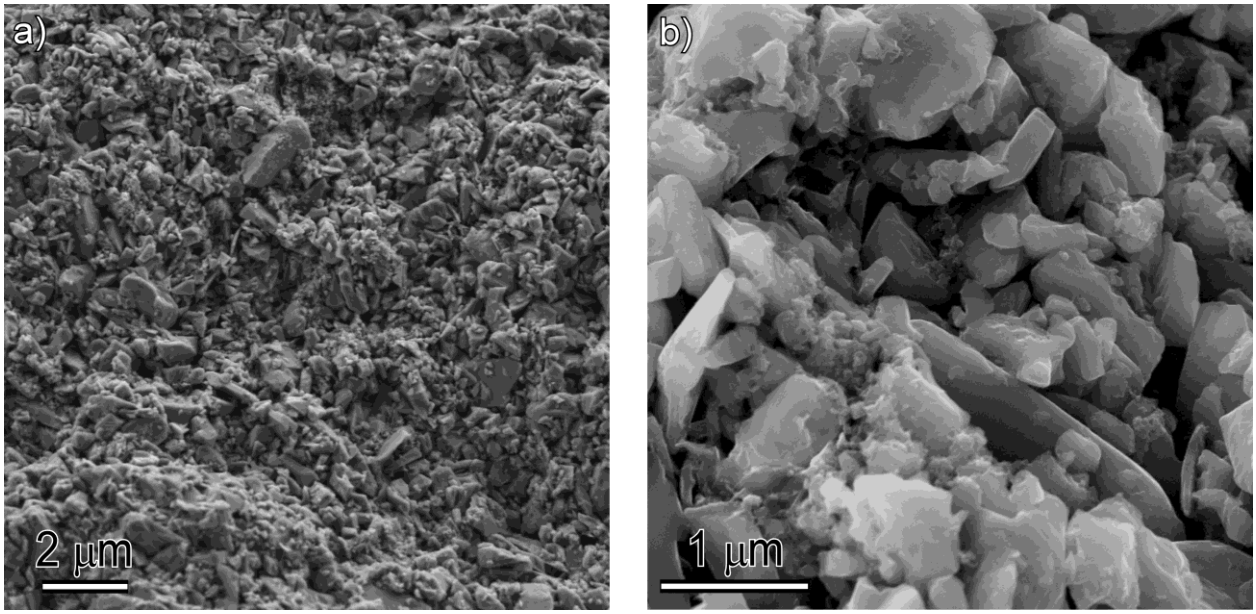

Figure 8: SE SEM micrographs of a green body pressed using uniaxial pressing at 27 MPa followed by CIP at 240 MPa, with the addition of a binder, reaching a green density of ~65%. The sample was fired at 1700°C for 30 minutes in flowing He.

A comparison of the green density obtained in each pressing method is shown in Figure 9.

An increase of ~5% in the green density was obtained by the combined uniaxial and CIP method.

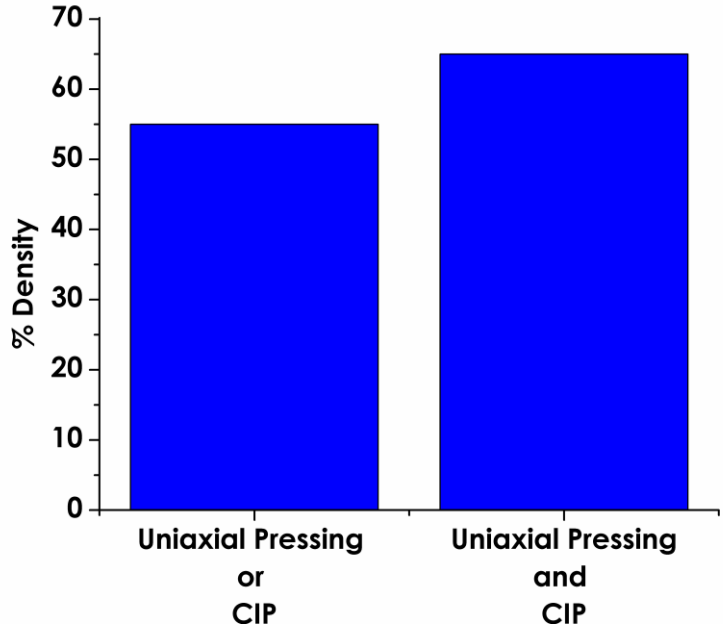

Figure 9: Comparison of the green density for each pressing method.

5.1.2 Sintering Experiments

The influence of powder processing can be seen in Figure 10, presenting SEM micrographs of the fracture surface of samples sintered at 2100°C for 30 minutes without additives. For the sample presented in Figure 10a no powder processing was done, and significant cracks and spherical aggregates can be seen. After powder processing, as presented in Figure 10b, a uniform microstructure is formed.

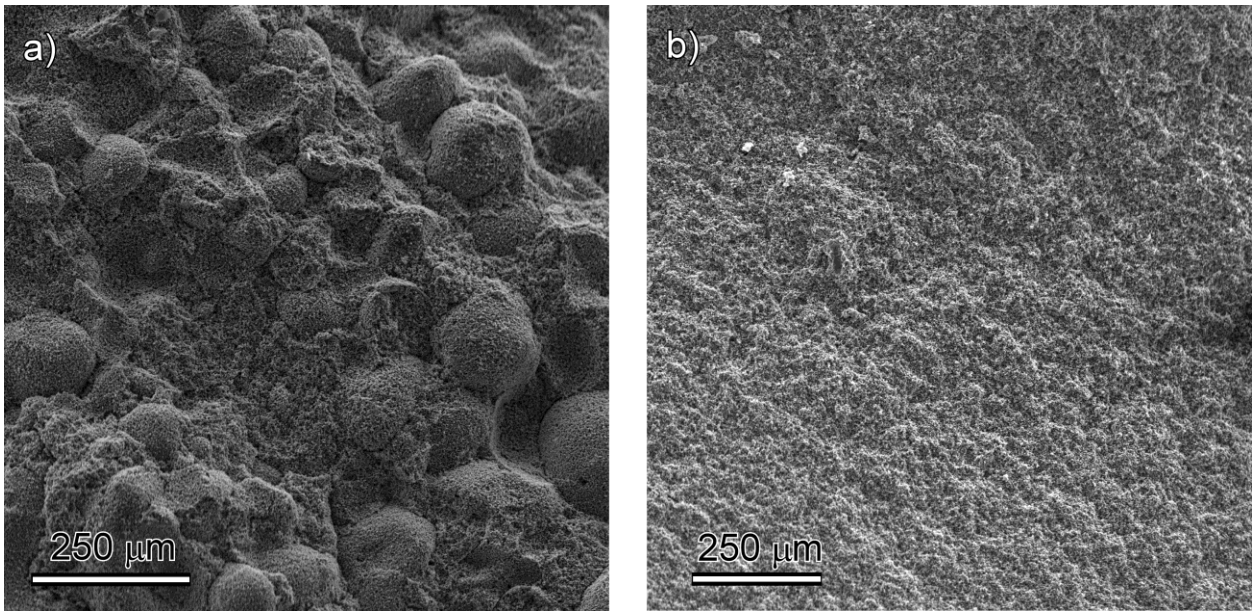

Figure 10: SE SEM micrographs, showing the fracture surface of SiC samples sintered at 2100°C for 30 min without the use of sintering additives after pressing by CIP: a) without powder processing; b) after powder processing.

Figure 11 presents SE SEM micrographs of SiC samples sintered without sintering additives at different sintering temperatures and times, listed in Table 4. The samples show a porous microstructure of interconnected pores and grains, with no or little increase in density (relative to the green body density). This morphology is often called a vermicular microstructure. The average grain size, pore size and neck width increases with increasing sintering temperature, and the grains are more faceted at higher sintering temperature. Longer sintering times for similar sintering temperatures (Figure 11c-d) result in larger necks and more faceted grains with little effect on the grain size. Isolated dense regions can be found in all the samples.

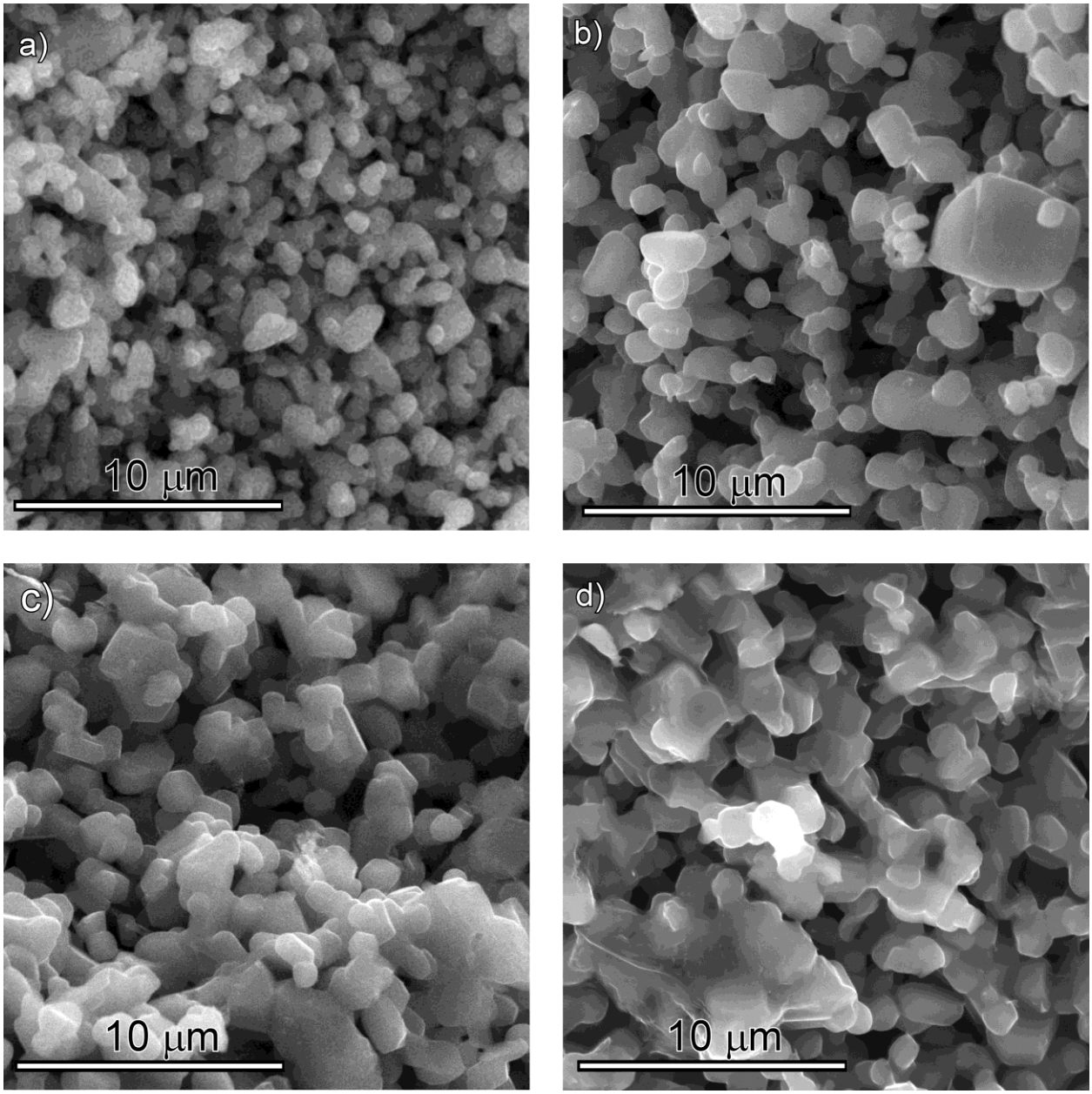

Figure 11: SE SEM micrographs of the fracture surface of SiC sintered without sintering additives, showing a coarse porous microstructure of interconnected grains of various sizes. a) Sintered at 1700°C for 30 min; b) sintered at 1900°C for 30 min; c) Sintered at 2100°C for 30 min; and d) Sintered at 2100°C for 3 hours.

Table 4: Density measurements of samples sintered without sintering additives at different temperatures and times.

	Temperature [°C]	Time	Density
1	1700	0.5	50
2	1900	0.5	50
3	2100	0.5	50
4	2100	3	55

Figure 12 presents TEM micrographs of a SiC sample, sintered without sintering additives at 2100°C for 30 minutes (also shown in Figure 11c). Figure 12a shows a crystalline SiC 6H grain in a $[2\bar{4}23]$ zone axis (marked with a yellow arrow) confirmed using electron diffraction (see the inset). An amorphous SiO_2 phase can be seen to be present between and over the SiC grains (marked with a red arrow), which was confirmed using EDS analysis (see Figure 13).

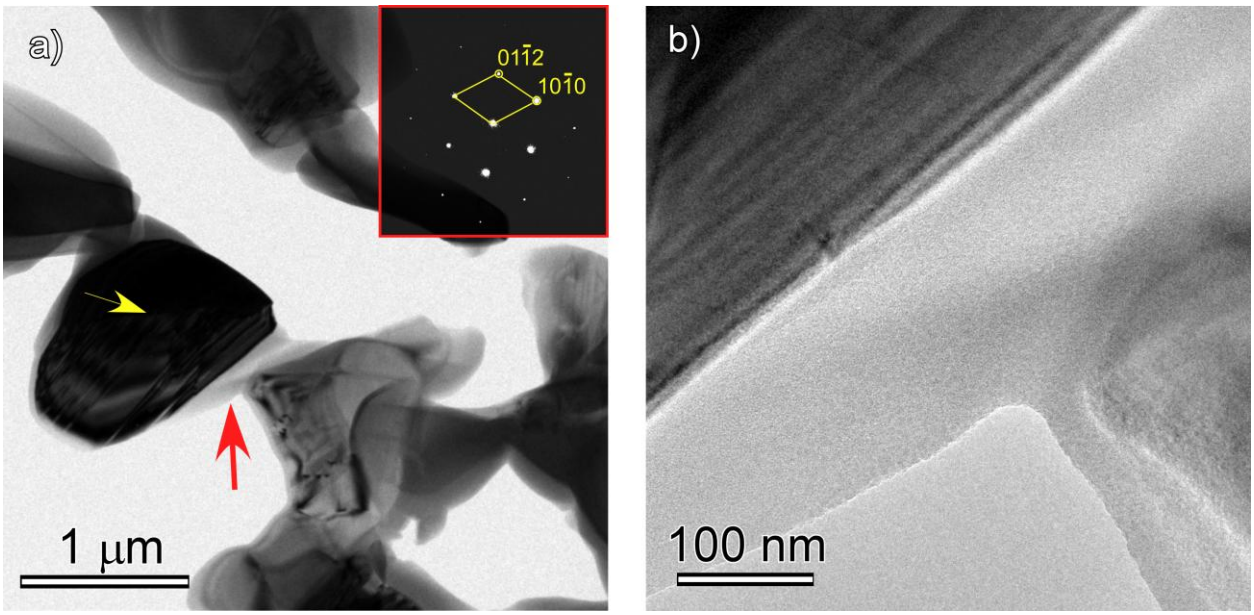

Figure 12: BF TEM diffraction contrast micrograph of a SiC sample sintered at 2100°C for 30min without the use of sintering additives. An amorphous SiO_2 phase (red arrow) was identified using EDS. a) Crystalline SiC grains with amorphous SiO_2 phase. The electron diffraction pattern of the arrowed (yellow arrow) grain shows the $[2\bar{4}23]$ zone axis of SiC 6H (shown in the inset). b) High magnification micrograph of the amorphous phase in a).

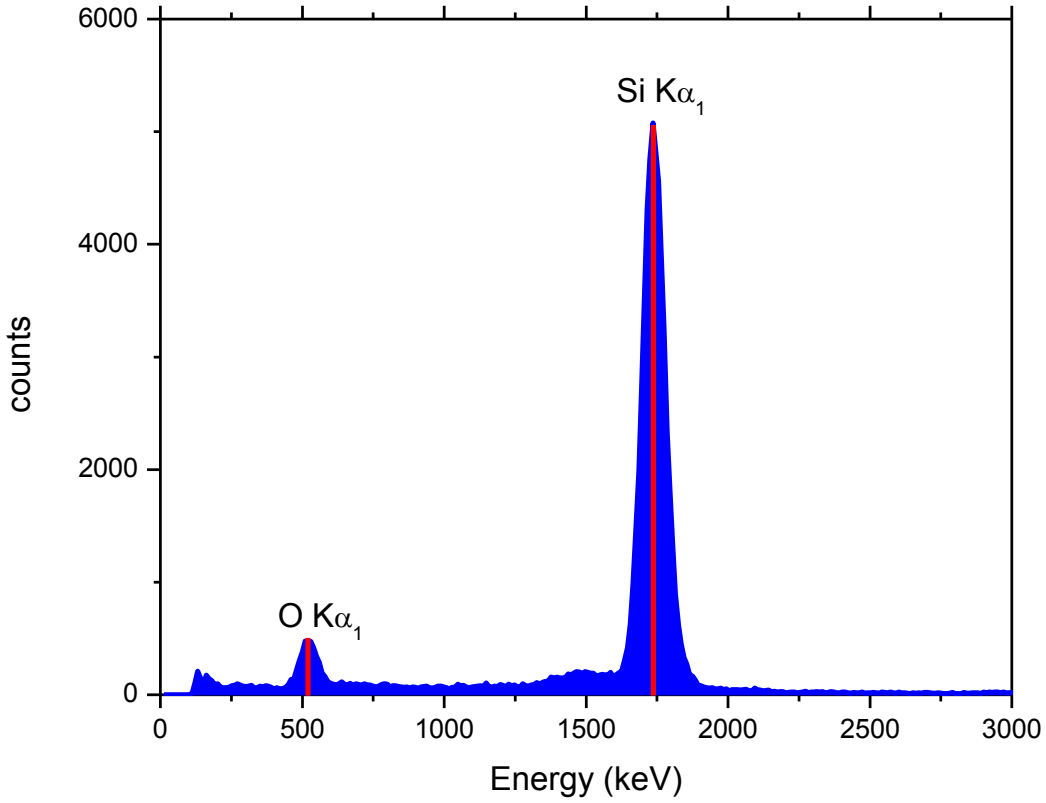

Figure 13: EDS spectrum of the arrowed area in Figure 12 showing the presence of SiO_2.

Figure 14 presents a SE SEM micrograph of the fracture surface of SiC samples sintered at 2100°C for 1 hour with 3wt.% carbon and 0.5 - 1 wt.% boron. While the sample sintered with 0.5 wt.% boron (Figure 14a) shows a characteristic trans-granular fracture mode, the sample sintered with 1 wt.% boron shows a characteristic inter-granular fracture mode with elongated grains. The density for both samples is presented in Table 5

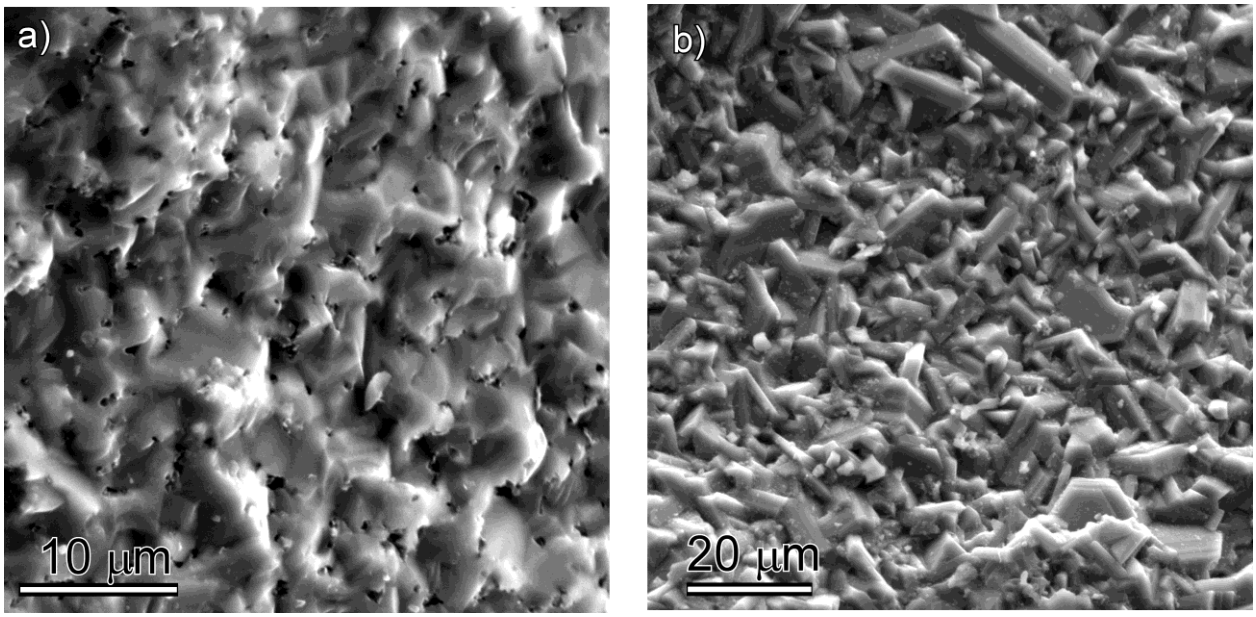

Figure 14: SE SEM micrographs (fracture surface) of SiC sintered at 2100°C for 1 hour with 3 wt.% carbon (6% phenolic resin) and a) 0.5 wt.% B, b) 1 wt.% B.

Table 5: Density measurements for sample sintered at 2100°C with 3 wt.% C and 0.5-1 wt.% B.

B (wt.%)	Density (%)
1	92±0.2
0.5	93±0.5

The influence of sintering temperature and time on the average grain size, density and microstructure was evaluated using a set of sintering experiments of varying temperature and time. Figure 15 presents SEM micrographs of SiC samples, sintered for 4 hours at 1950°C, 2050°C and 2100°C, showing an increase in grain size and a decrease in pore size with increasing sintering temperature. The formation of a few elongated grains appears only at 2100°C. Noticeable surface faceting was present due to the thermal etching of the samples [18].

The average grain size for the set of samples that was sintered at 2100°C is shown in Figure 16**,** indicating a slight increase in the grain size given the standard error of the grain size after

4 hours. The density measurements for samples sintered at different temperatures and times can be found in Figure 17**,** showing an increase in density as a function of both sintering temperature and time, reaching a maximum of 96%.

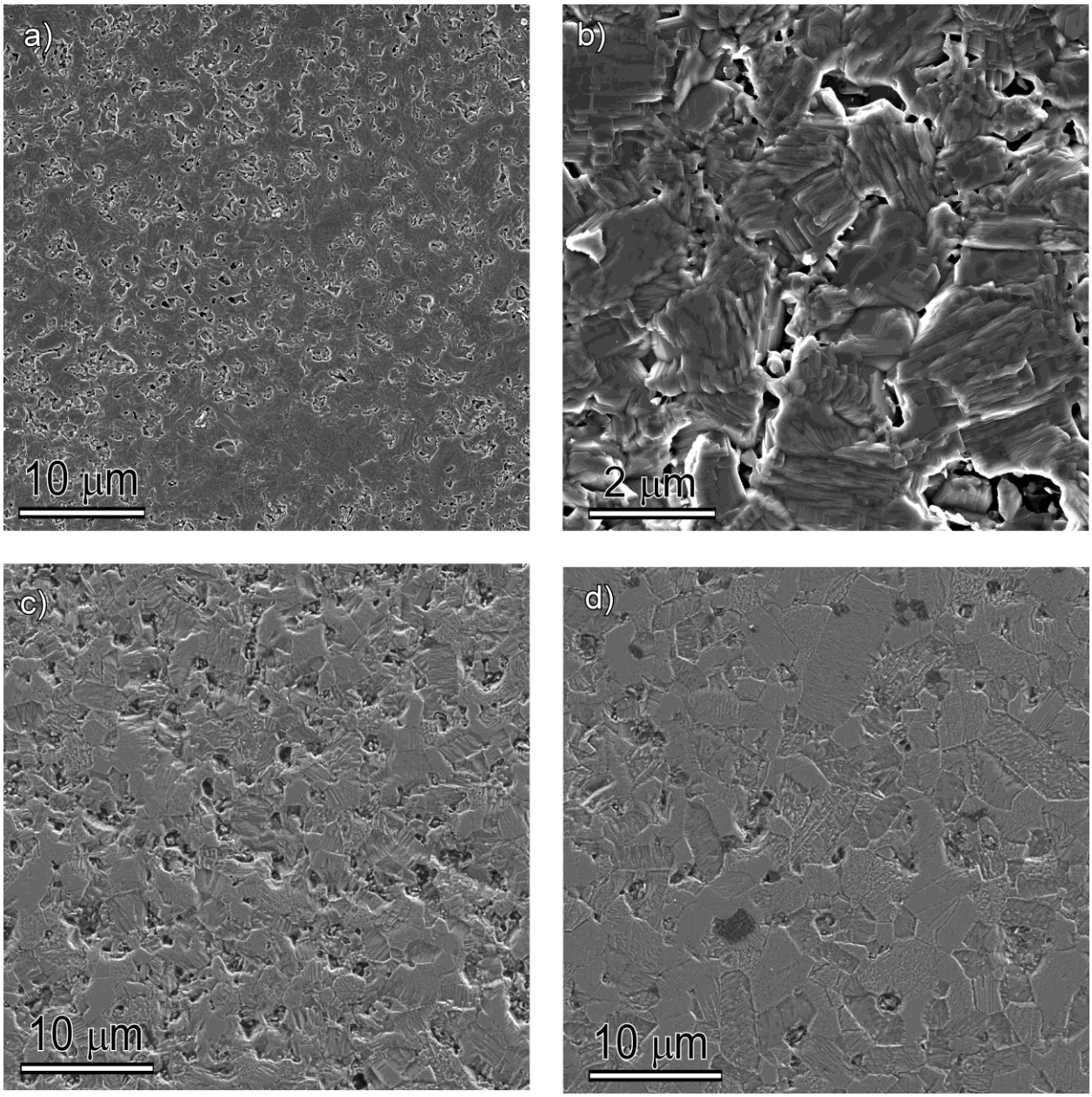

Figure 15: SE SEM micrographs (polished and thermally etched) of SiC doped with 0.5 wt.% B and 6 wt.% C for 4 hours at various temperatures: a-b) 1950°C; c) 2050°C; d) 2100°C.

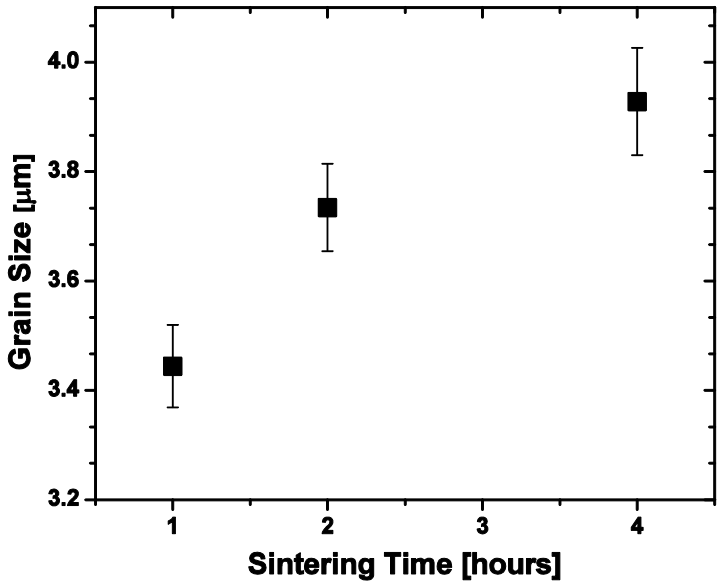

Figure 16: Grain size measurement for SiC samples sintered at 2100°C for different times, doped with 0.5 wt.% B and 3 wt.% C.

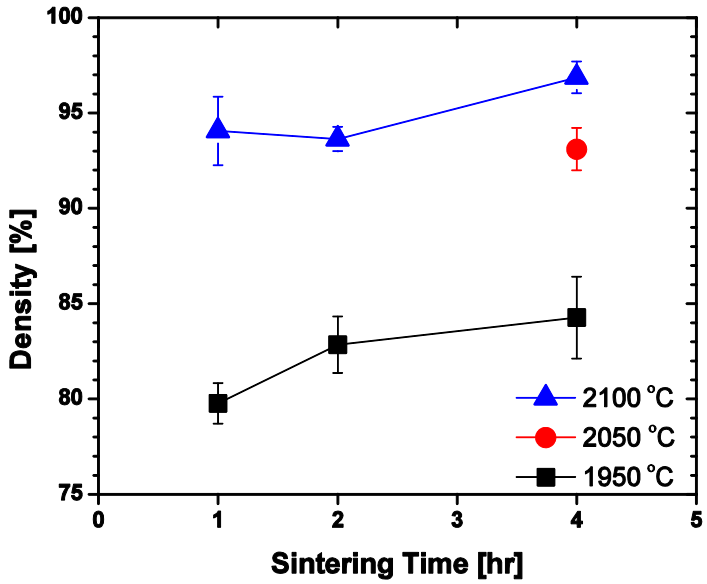

Figure 17: Density measurements for SiC samples doped with 0.5 wt.% B and 3 wt.% C at different sintering temperatures and time.

Figure 18 presents SEM micrographs of SiC sintered at 2100°C for 1 hour without the addition of carbon, showing a porous microstructure with interconnected grains similar to the one shown in Figure 11. The density for this sample reached ~65%, close to the density of the green body.

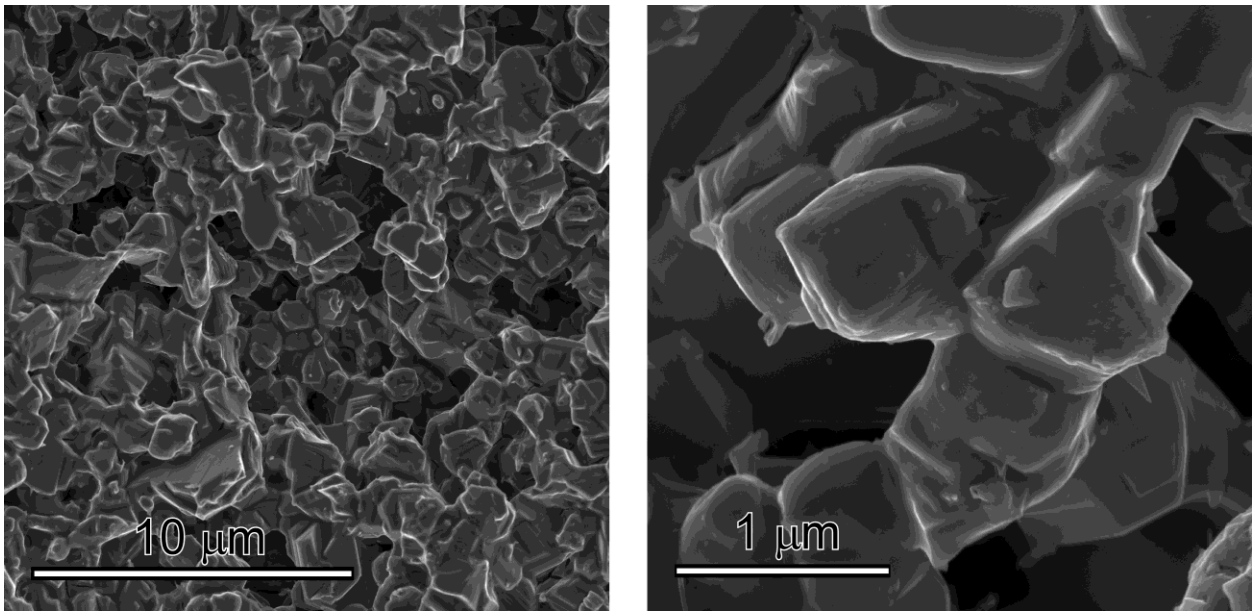

Figure 18: SE SEM micrographs (fracture surface) of SiC sintered at 2100°C for 1hr, doped with 0.5 wt.% B.

Figure 19 presents a SE SEM micrographs of a SiC sample, sintered at 2100°C for 1 hour without the addition of boron, showing a porous microstructure with flake-like structures on the surface of the grains. The density of this sample reached ~55%, similar to the density of the green body and other samples sintered without sintering additives. The sample was pressed using only CIP without the use of uniaxial pressing since no binder (which is the main source for carbon) could be added. TEM analysis of this sample is presented in Figure 20, showing SiC and an amorphous phase (arrowed) of varying compositions of $Si_xO_yC_z$, Si_xO_y, and Si, determined using EDS, from a similar flake-like feature as shown in Figure 19,

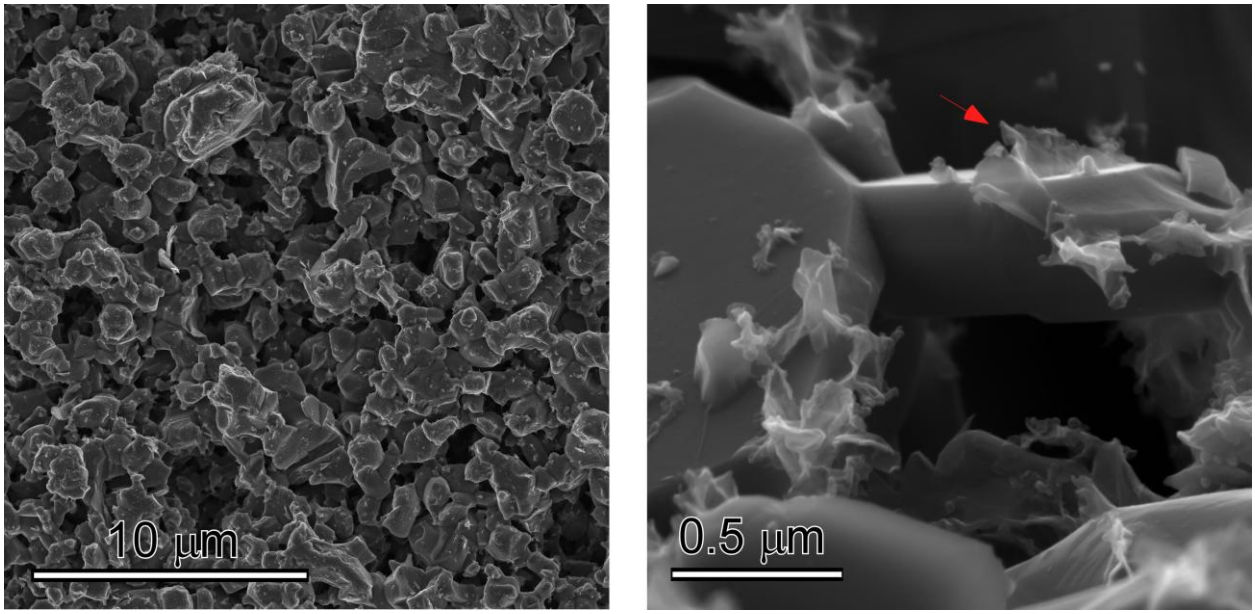

Figure 19: SE SEM micrographs (fracture surface) of SiC sintered at 2100°C for 1hr, doped with 3 wt.% C, showing porous microstructure and flake like features (arrowed) on the surface of the grains.

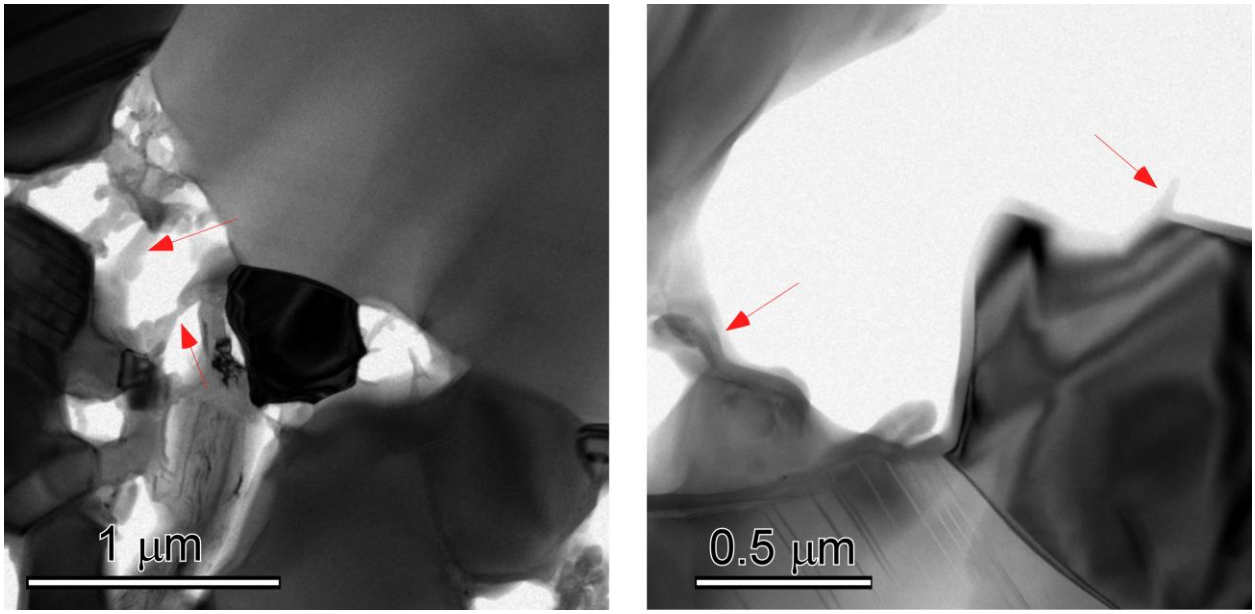

Figure 20: BF diffraction contrast TEM micrographs of SiC sintered at 2100°C for 1hr, doped with 3 wt.% C. The arrowed areas are amorphous phases (determined using electron diffraction) of varying compositions of $Si_xO_yC_z$, Si_xO_y, and Si.

5.2 Reduction Experiments

TEM of the plan-view sample immediately after ion milling is presented in Figure 21a showing a ~2nm thick amorphous layer along the edge of the sample, caused by the ion milling process [20]. After the oxidation process, a ~30 nm thick amorphous layer is visible

along the edge of the sample as shown in Figure 21b. The transition from the amorphous to crystalline region was confirmed directly from the HRTEM micrographs (Figure 21c), and from fast Fourier transforms (FFT) of regions of the micrograph shown in Figure 21b. After coating the oxidized TEM sample with carbon and annealing at 1400°C in He, the amorphous SiO_2 was reduced, as shown in Figure 21d.

Figure 22 presents a cross-section TEM analysis of the oxidized bulk wafer, annealed in air at 1100°C, showing a ~17 nm thick amorphous layer on the surface of the wafer. EDS confirmed this layer to be SiO_2 as shown in Figure 23. The epoxy used for sample preparation, and the SiC layer, were also identified by EDS.

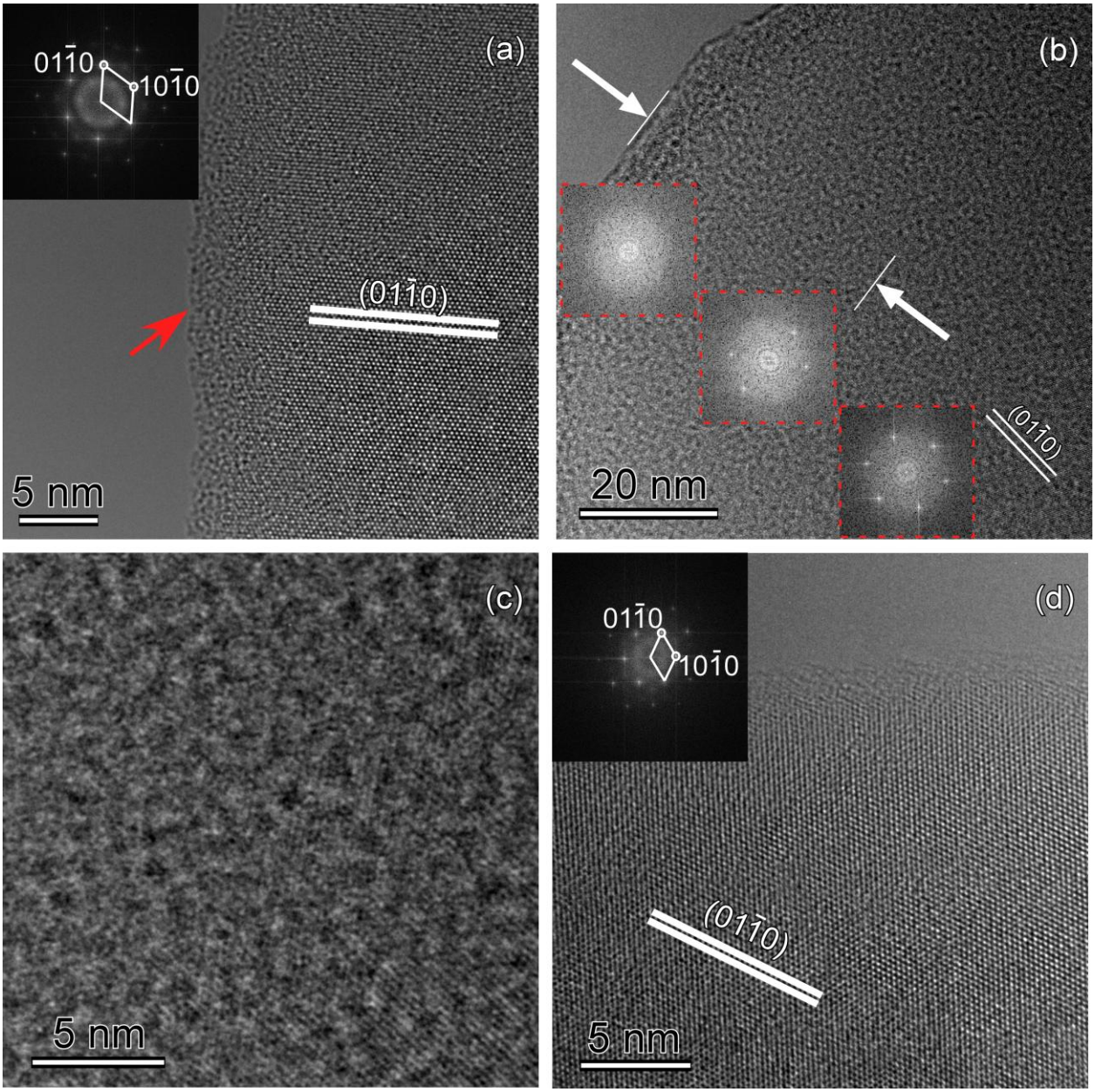

Figure 21: HRTEM micrographs of a plan-view sample of single crystal SiC in the [0001] orientation, (a) immediately after preparation, showing a ~2nm thick amorphous layer due to ion milling; (b) after oxidation at 1400°C, showing ~30 nm amorphous layer, the transition from amorphous to crystalline can be seen using the FFT analysis (shown on the micrograph); and by (c) high magnification of the transition area. (d) After carbon coating and reduction at 1400°C, showing a ~1nm thick amorphous layer.

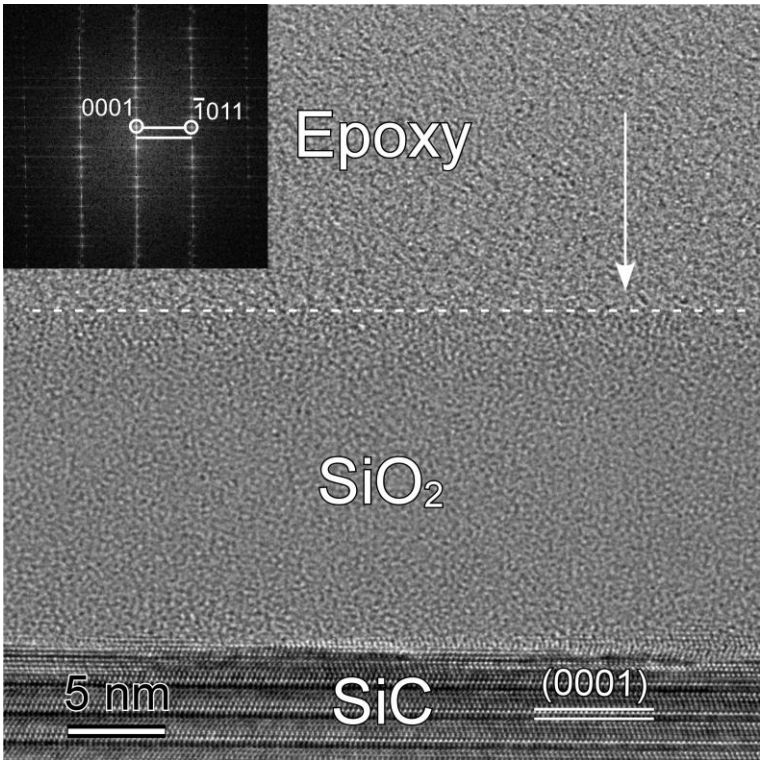

Figure 22: HRTEM micrograph of a cross-section oxidized (at 1100°C) SiC single crystal wafer in a [$\bar{1}2\bar{1}0$] zone axis, showing ~17nm thick amorphous layer on the surface of the wafer.

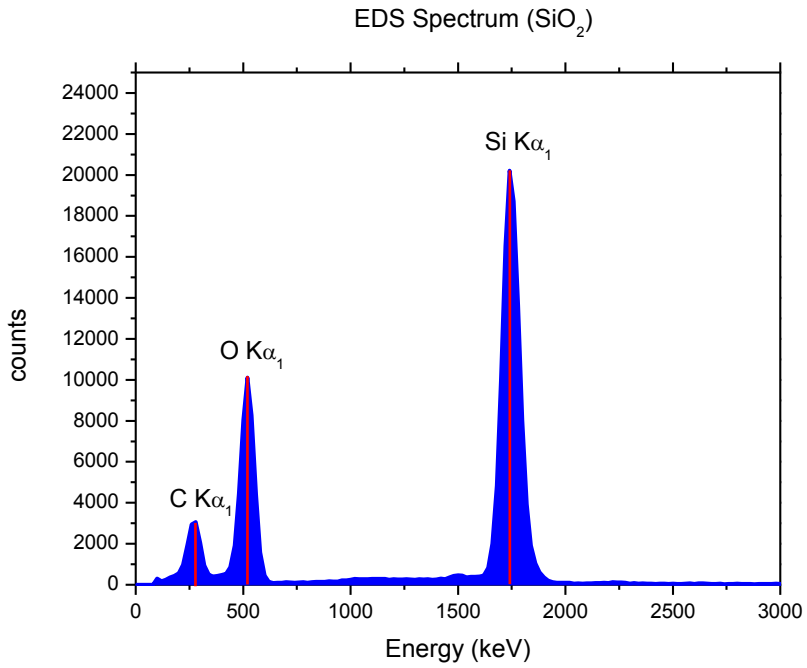

Figure 23: EDS analysis of the amorphous layer, shown in Figure 22.

TEM and SEM micrographs from the same area of the reduced plan-view sample are presented in Figure 24. The edge of the sample was thickened in several places, partially covered with an amorphous SiO_2 layer, confirmed using electron diffraction and EDS. Hexagonal holes and surface faceting are also present on the surface of the sample. Ni contamination (confirmed by EDS) is also present on the surface at various locations, originating from the reduction furnace.

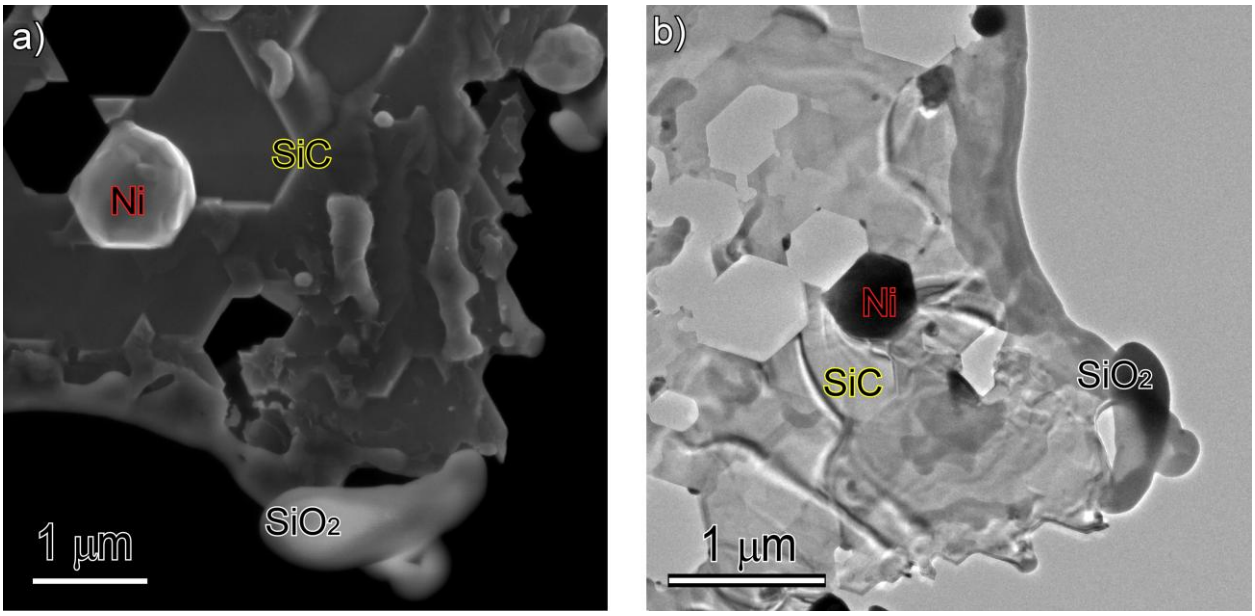

Figure 24: Micrographs of a reduced (at 1400°C) plan-view sample: a) SE SEM micrograph; b) BF TEM micrograph. Both micrographs show the same region of the sample (mirror inversion). The edge of the sample is partially covered with a thick SiO_2 layer. Ni contaminants are also present on the surface.

Figure 25 presents SE SEM micrographs of a reduced wafer. While most of the wafer contains no detectable topography, a few isolated circular areas of different size were found, as shown in Figure 25a. Each large circular area contains two different regions: a center region with relatively deep pits and an outer region with pinholes and shallow trenches and steps.

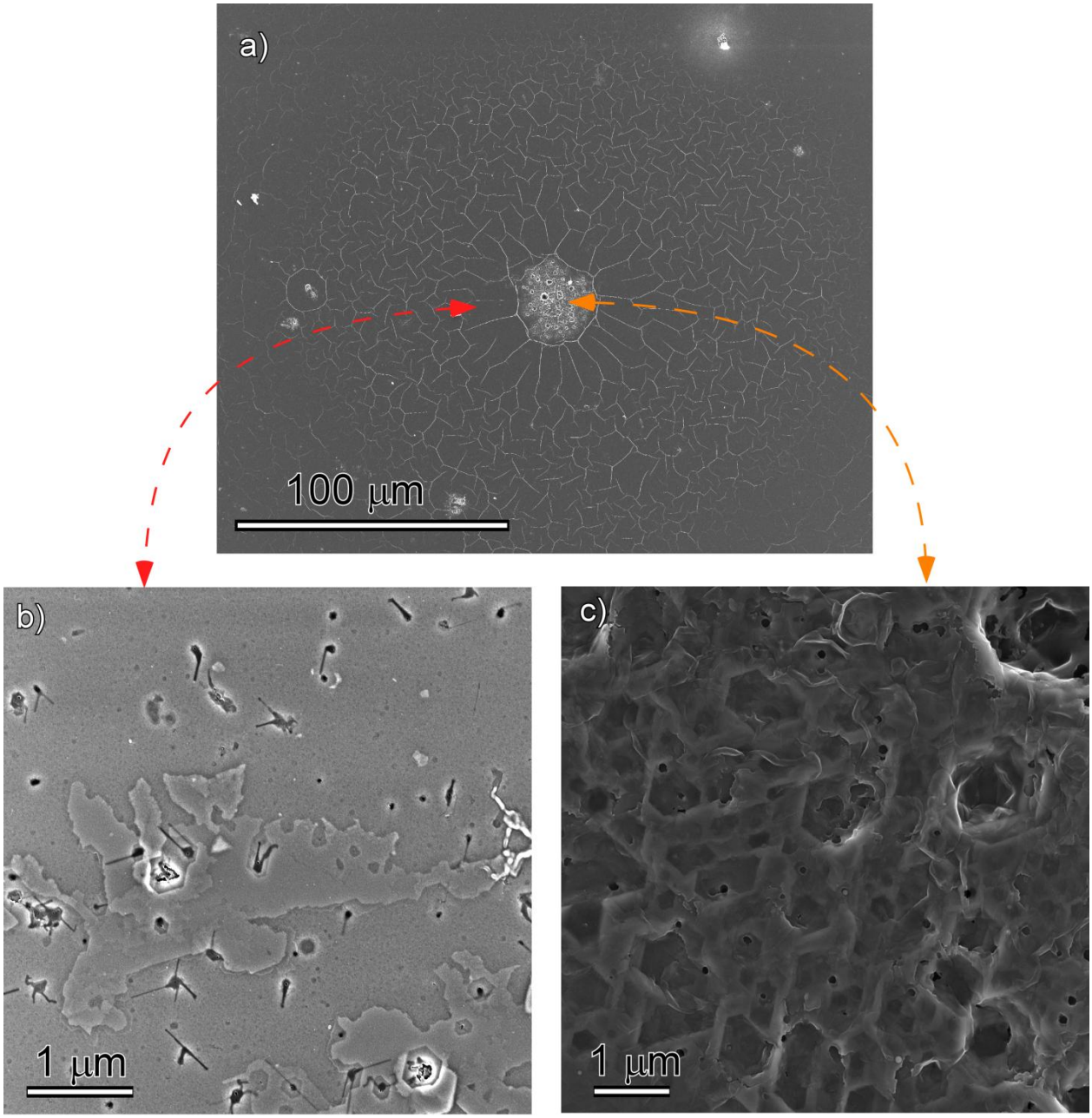

Figure 25: SE SEM micrographs of a reduced (1400°C) SiC single crystal wafer showing: a) the circular crater-like feature; b) high magnification of the outer region (arrowed); and c) high magnification of the inner region (arrowed).

6 Discussion

6.1 Sintering Process

6.1.1 The Influence of Powder Processing on the Green Body

The results presented in section 5.1.1 show the presence of agglomerated powder particles and their influence on the sintering process. Agglomerates are naturally occurring conglomerated powder grains caused by either chemical reaction between the powder grains during the powder manufacturing process (hard agglomerates), or by an electrostatic attraction between the powder grains (soft agglomerates). An individual agglomerate can be regarded as a green body with a high green density, since the pressure required to mechanically break it can reach up to several tens of GPa [21], which cannot be achieved by uniaxial pressing or CIP methods used here. The agglomerates therefore remain whole inside the green body, causing the microstructure schematically illustrated in Figure 26 to form, due to large inter-agglomerate pores that cannot be eliminated during sintering. By the process of ball-milling and the use of a deflocculant, most of the agglomerates are eliminated, and a uniform close-packed microstructure is formed.

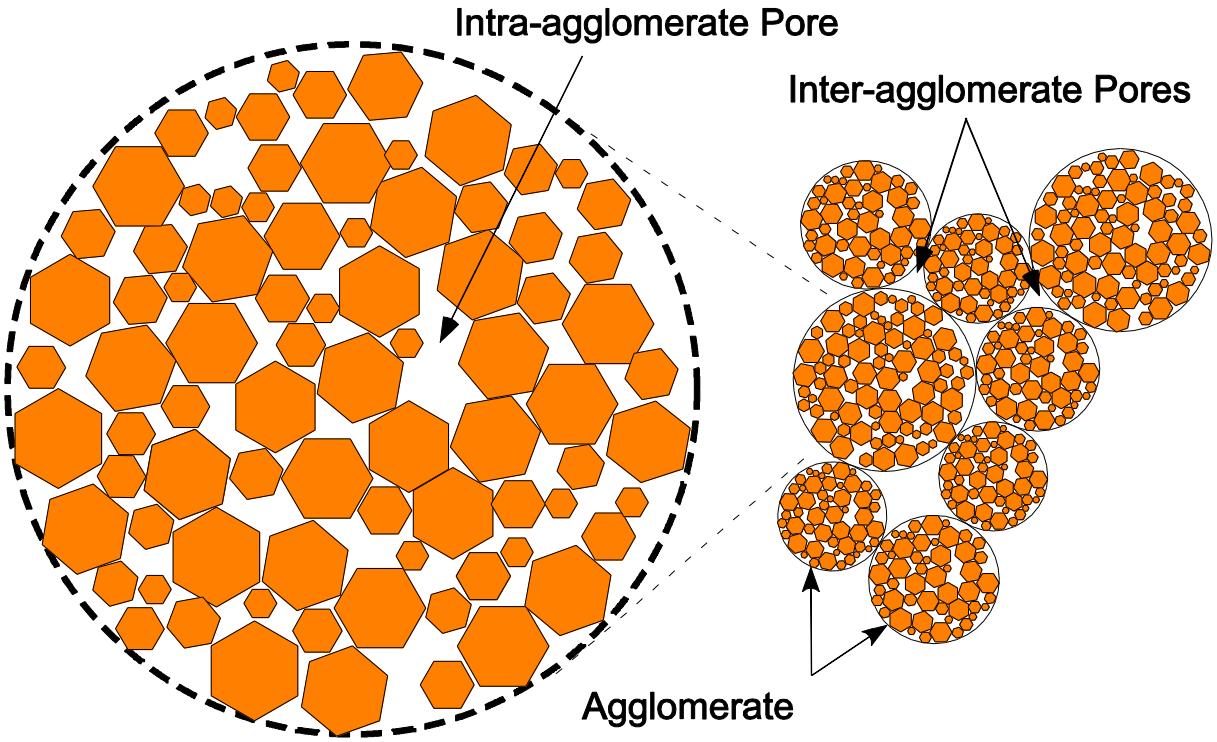

Figure 26: Schematic illustration of the microstructure of an individual agglomerate containing intra-agglomerate pores, and the microstructure of the green body formed from an agglomerated powder, containing inter-agglomerate pores

6.1.2 The Influence of Compaction Method on the Green Body Density

As presented in section 5.1.1, uniaxial pressing allows a good control of the two-dimensional geometry of the sample, which is important for industrial applications. However, the applied uniaxial stress results in an asymmetric density profile across the ample as illustrated in Figure 27 [22]. The presence of a density profile induces a stress gradient which causes the separation of areas of uniform density from each other. The addition of a binder joins the grains together, allowing a better resistance to the internal stresses, thus increasing the critical point of the density difference for the separation of equal density areas, reducing the amount of separated parts inside the green body.

The cold isostatic pressing method was extensively used for all the green bodies produces in this work due to the high pressure that can be applied and the good physical properties of the green body. The CIP process creates a uniform density profile in the green body, and hence

is nearly stress-free. Using CIP on a uniaxially pressed green body eliminates much of the existing stress, while including the good control on the sample geometry from uniaxial pressing.

The increase of the green density by the combined uniaxial and CIP method can be explained as the result of a good particle arrangement during the uniaxial step, during which the particles are under shear and compression stress, and the good compaction due to the compressive stress applied during CIP.

The use of a lubricant enhances the densification process by lowering the friction between the powder grains, allowing a better rearrangement at a lower pressure, thus reaching a better compaction and higher green density.

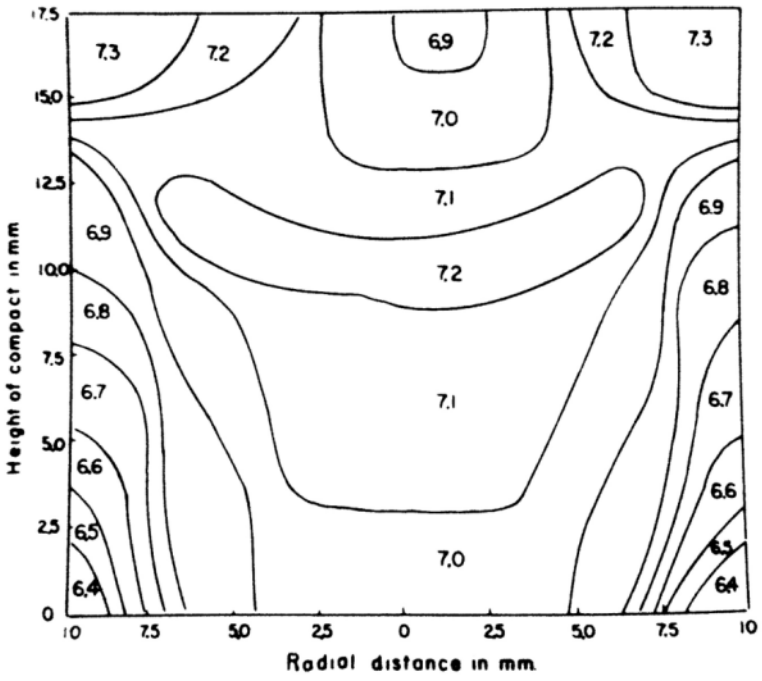

Figure 27: Illustration of the density profile inside a uniaxially pressed green body (redrawn from [22]).

6.1.3 The Influence of Sintering Temperature and Time

The results presented in section 4.1.3 show the influence of the sintering temperature and time on the density of the sintered samples, where longer sintering times and higher sintering temperatures result in higher sintering densities. Increasing the sintering time from 1 to 4 hours affects the density by 3-4%; increasing the sintering temperature by 150°C improves the density by 10%. This result is expected, since any kinetic mechanism (including sintering) will increase in rate as a function of both time and temperature [8]. However, the increase in density is seen only for the boron and carbon doped samples. For undoped samples, or samples containing only one dopant (boron or carbon), the density is affected by neither temperature nor time.

A log-normal grain size distribution is presented in Figure 28 for the sample sintered at 2100°C for 4 hours, indicating a normal grain growth mechanism [23]. Despite that, a few slightly elongated grains could be detected in this sample (Figure 15).

The effective growth rate and grain boundary mobility of SiC were not measured is this work, as each measurement of the average grain size was conducted on a different specimen and the average grain size at t=0 was not measured. The results thus show a qualitative dependence of the growth rate as function of time.

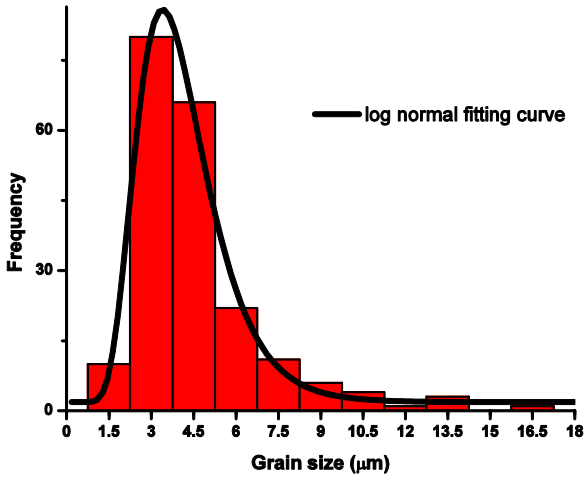

Figure 28: Grain size distribution and a log-normal fitting curve analysis for a SiC sample doped with carbon and boron, sintered at 2100°C for 4 hours.

6.1.4 The Influence of Sintering Additives on the Microstructure

The role of the sintering additives on pressureless sintering of SiC is crucial; the addition of both carbon and boron in sufficient amounts is required to activate densification. Otherwise, a coarse and porous vermicular microstructure will result, with no or very little densification.

The formation of the vermicular microstructure is often described as the result of a kinetic mechanism in which high surface (or vapor) diffusion rates together with low grain boundary (and volume) diffusion rates, promote coarsening and inhibit densification [12, 24]. The low volume diffusion rate is explained as a result of the covalent nature of Si-C bonds, causing a high activation energy for the formation of volume defects, which participate in volume diffusion. However, even if this is true for volume diffusion, it is clear that this is not the case for grain boundaries where a high concentration of defects exists, facilitating grain boundary diffusion. Since SiC-SiC grain boundaries are formed in a dopant free material the absence of densification cannot be explained solely as resulting from a kinetic diffusion issue.

As will be discussed, this phenomenon might be common for covalent solids due a different reason than low diffusion rates.

A green body with a low green density may also be a reason for a coarse porous microstructure. In this case, densification is inhibited due to the large intergranular distances and coarsening occurs at high rate, due to poorly arranged grains with a low coordination number and large pores [25]. However, it is clear that the green body produced by the method shown in this work is not the cause, since a high density was achieved with the addition of carbon and boron, using green bodies prepared by exactly the same method.

The (bulk) SiO_2 film in the dopant free sample, as shown in Figure 12, can be explained as originating from initial surface of the powder particles, since the low $P(O_2)$ used for the sintering process should limit oxidation of SiC. SiC and SiO_2 react at elevated temperatures, forming volatile products [15]; the presence of SiO_2 film after sintering indicates that this reaction occurs at a slow rate that does not remove significant amounts of SiO_2 from the surface, within the time frame of the process used here.

A boron concentration of 0.5 wt.% was selected for the sintering process since higher boron concentrations lead to elongated grains and transgranular fracture, as shown in Figure 14b. Stobierski and Gubernat also studied this phenomenon and showed that high concentrations of boron cause rapid sintering (samples reaching 90% density in 1 minute) with elongated grain growth and pore occlusions [14]. An intergranular fracture mode in the absence of a secondary phase (as in this case) results from "weaker" grain boundaries, which should be avoided.

Without the use of carbon (only boron), a porous microstructure was formed, similar to the dopant free SiC, indicating that boron activates the densification process only in the presence of carbon. However, without the use of boron (only carbon), a slightly different porous microstructure results, with the formation of a flake-like morphology of an amorphous phase on the surface of grains, as shown in Figure 20. The silicon oxi-carbide composition of varying stoichiometry of this amorphous phase indicates that carbon reacts with the surface SiO_2, and in the absence of boron, forms this amorphous phase which covers the grains and inhibits densification in a similar manner to that of SiO_2.

6.2 Reduction Experiments

The results presented in section 5.2 show the role of carbon during the sintering of SiC as a reducing agent for SiO_2. The purpose of the model oxidation/reduction experiments was to model the oxide layer on SiC powder grains, originating either from surface oxidation or manufacturing contamination [26]. The results presented in Figure 21 show the reduction of a thermally grown surface SiO_2 by the addition of carbon.

By using a plan-view sample for the model experiment, direct characterization for each of the experimental steps on the same sample at multiple locations across the sample is possible. The drawback of this method is the thickening of the thin edge of the sample during the thermal treatments as a result of surface diffusion and the driving force for the reduction of surface area, which reduces the accuracy of the TEM analysis. Comprehensive characterization from different directions and at different length-scales was achieved by combining the information from different samples (cross-section and wafer).

The results presented in Figure 21 shows the reduction of (bulk) surface SiO_2 on SiC. However, the results shown in Figure 20, Figure 24, and Figure 25 may also suggest that the reduction of SiO_2 (as in equation (4)), may be one of a larger set of reactions that occur during the thermal process, since the entire oxygen containing amorphous layer not is removed. Also, as shown in Figure 20, amorphous phases containing oxygen, silicon, and carbon, remain in the sample after sintering at 2100°C with the addition of only carbon. This indicates that while the added amount of carbon is sufficient for the activation of densification, this reduction process is not sufficient to remove all of the oxygen from the surface of SiC.

The hexagonal shaped pits shown on the reduced samples may result from oxidation of the SiC single crystal, along dislocation lines and preferred crystallographic directions [27,28]. The large circular crater shown in Figure 25 is explained as resulting from the oxidation step, during which a metastable cristobalite forms. Since oxygen diffuses slower through cristobalite than in amorphous SiO_2 and the precipitate is gradually growing from the nucleation point at the center, an oxidation profile is formed in the substrate (Figure 29) [29]. After reduction of the surface SiO_2 the structure of the underlying SiC is exposed, revealing the anisotropic oxidation of SiC as shown in Figure 25.

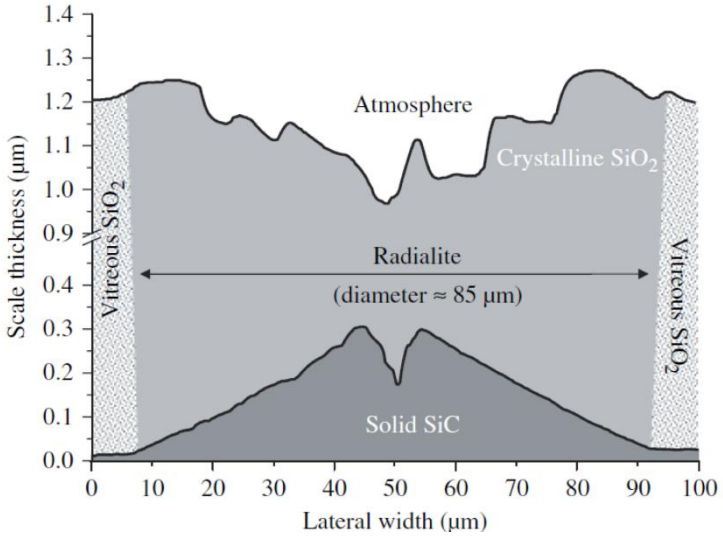

Figure 29: Oxide layer profile caused by the formation of a cristobalite precipitate [29].

6.3 SiO_2 Densification Inhibition Mechanism

The inhibition of densification of SiC in the presence of small amounts of SiO_2 in can be explained by considering the surface energies of the system. The main driving force for sintering is the replacement of free surface area by lower energy grain boundaries. SiC has an anisotropic equilibrium crystal shape, where the (0001) surface is considered to have the lowest surface energy, ~1620 mJ/m^2 [30]. Assuming that the grain boundary energy in polycrystalline SiC is between 0.3-0.5 of that of the free surface, the lower range of grain boundary energy should be 486-810 mJ/m^2. However, the surface energy of SiO_2 is quite low, in the range of 307 mJ/m^2 [31]. As such, oxidation of the SiC surface implies a significant reduction of the free surface energy, and reduction of the driving force for sintering. As described schematically in Figure 30, the reduction of the total surface energy of the system would therefore only be achieved by reducing the total surface area rather than replacing free surfaces with grain boundaries via densification, which explains the significant particle coarsening which occurs in the undoped samples.

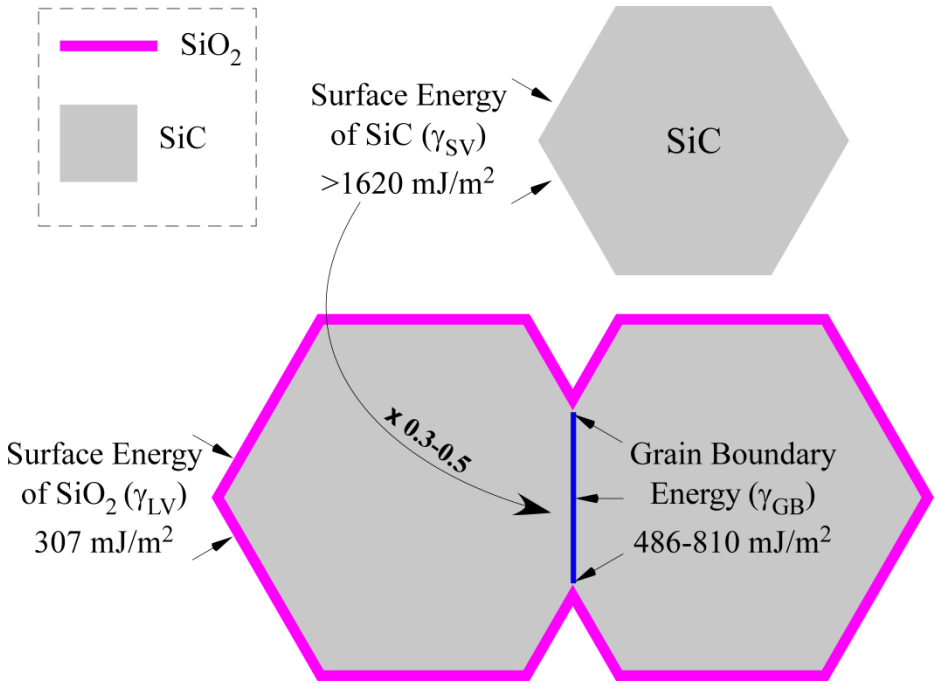

Figure 30: The surface energies in the SiC/SiO_2 system.

If enough SiO_2 formed, then the system could sinter via liquid-phase sintering, resulting in a two-phase body composed of SiC and SiO_2 [32]. However, within the time-frame and temperatures of the experiments conducted here, the (limited) passivation of SiO_2 and the relatively low oxygen partial pressure of the sintering atmosphere limit the total amount of SiO_2 formed. As such, sintering is prevented by the thin oxide film on the SiC particles.

This study directly confirms that carbon is required to reduce native SiO_2 on the surface of SiC [15]. The presence of a wetting film of SiO_2 on the SiC particles reduces the driving force for densification.

7 Summary and Conclusions

A pressureless solid state sintering process for silicon carbide was developed in this work. A high sintered density of ~96% was reached using 0.5 wt.% boron and 3 wt.% carbon as sintering additives. Sintering SiC without additives resulted in a porous vermicular microstructure consisting of interconnected pores and grains, with an amorphous SiO_2 film between the grains. The influence of sintering temperature, time and additives on the microstructural evolution were studied.

The role of carbon in the reduction of SiO_2 from the surface of SiC was directly shown using a model experiment, where thermally oxidized SiC single crystals were coated with carbon and then thermally annealed, reducing the thermally grown SiO_2.

The thermodynamic mechanism by which SiO_2 on the surface of SiC inhibits densification in dopant free SiC was proposed to be the (significant) reduction of free surface energy, resulting in a reduction of the thermodynamic driving force for densification, allowing only microstructural coarsening to take place.

8 Recommendation for Future Work

The actual mechanism by which boron contributes to densification during the pressureless solid state sintering of SiC was not evaluated in this work and should be the focus for future studies by using a similar experimental approach. However, it may be postulated that the fundamental physical role is similar to that of carbon, where the reaction of boron with residual graphite on the surface of SiC (due to surface graphitization [33]) removes the low surface energy graphite.

The solubility of boron in SiC should be determined at the temperatures of interest. If the added boron is in the form of a solid solute (below the solubility limit), it might reduce the grain boundary energy by the formation of a boron-based complexion [34]. If it is above the solubility limit (as a precipitate), it might react with carbon, enabling the complete removal of the surface oxides and graphite as discussed above. According to the results of the solubility limit measurements, a model experiment can be done, that will show the presence of boron in a boron enriched complexion and its influence on the surface energies, or the reaction between boron and the residual amorphous phase (as shown in Figure 20) in a carbon doped SiC.

A comprehensive understanding of the physics of the sintering process of SiC and the exact roles of the sintering additives is essential not only for SiC, but also for other materials such as Si_3N_4 and B_4C that exhibit similar sintering behaviors [12,24].

9 References

1. C. E. Anderson Jr, T. Behner, T. J. Holmquist, D. L. Orphal, Penetration response of silicon carbide as a function of impact velocity, International Journal of Impact Engineering, 38[11]:892-899, 2011.
2. E. Gomez, J. Echeberria, I. Iturriza, F. Castro, Liquid phase sintering of SiC with additions of Y2O3,
2. E. Gomez, J. Echeberria, I. Iturriza, F. Castro, Liquid phase sintering of SiC with additions of Y2O3, Al2O3 and SiO2, Journal of the European Ceramic Society, 24[9]:2895-2903, 2004.
3. L. L. Snead, T. Nozawa, Y. Katoh, T.-S. Byun, S. Kondo, D. A. Petti, Handbook of SiC properties for fuel performance modeling, Journal of Nuclear Materials, 371[1–3]:329-377, 2007.
4. S. Prochazka, R. M. Scanlan, Effect of Boron and Carbon on Sintering of SIC, Journal of the American Ceramic Society, 58[1-2]:72-72, 1975.
5. W. Y. Ching, Y.-N. Xu, P. Rulis, L. Ouyang, The electronic structure and spectroscopic properties of 3C, 2H, 4H, 6H, 15R and 21R polymorphs of SiC, Materials Science and Engineering: A, 422[1–2]:147-156, 2006.
6. P. Shaffer, A review of the structure of silicon carbide, Acta Crystallographica Section B, 25[3]:477-488, 1969.
7. J. A. Lewis, Colloidal Processing of Ceramics, Journal of the American Ceramic Society, 83[10]:2341-2359, 2000.
8. S.-J. L. Kang. I - Sintering Processes. In: Kang S-JL, editor. Sintering. Oxford: Butterworth-Heinemann, 2005. p.3-8.
9. F. F. Lange, Hot-pressing behaviour of silicon carbide powders with additions of aluminium oxide, Journal of Materials Science, 10[2]:314-320, 1975.
10. M. Mitomo, Y.-W. Kim, H. Hirotsuru, Fabrication of silicon carbide nanoceramics, Journal of Materials Research, 11[07]:1601-1604, 1996.
11. F. F. Lange, T. K. Gupta, Sintering of SiC with Boron Compounds, Journal of the American Ceramic Society, 59[11-12]:537-538, 1976.
12. C.Greskovich, J. H. Rosolowski, Sintering of Covalent Solids, Journal of the American Ceramic Society, 59[7-8]:336-343, 1976.
13. L. Stobierski, A. Gubernat, Sintering of silicon carbideI. Effect of carbon, Ceramics International, 29[3]:287-292, 2003.
14. L. Stobierski, A. Gubernat, Sintering of silicon carbide II. Effect of boron, Ceramics International, 29[4]:355-361, 2003.
15. W. J. Clegg, Role of Carbon in the Sintering of Boron-Doped Silicon Carbide, Journal of the American Ceramic Society, 83[5]:1039-1043, 2000.
16. H. Ye, G. Rixecker, F. Aldinger. Liquid Phase Sintered SiC with SiO2 Additive. Ceramics – Processing, Reliability, Tribology and Wear. Wiley-VCH Verlag GmbH & Co. KGaA, 2006. p.172-177.
17. R. Vassen, D. Stöver, Processing and Properties of Nanograin Silicon Carbide, Journal of the American Ceramic Society, 82[10]:2585-2593, 1999.

18. N. G. van der Berg, J. B. Malherbe, A. J. Botha, E. Friedland, Thermal etching of SiC, Applied Surface Science, 258[15]:5561-5566, 2012.
19. M. I. Mendelson, Average Grain Size in Polycrystalline Ceramics, Journal of the American Ceramic Society, 52[8]:443-446, 1969.
20. Á. Barna, B. Pécz, M. Menyhard, TEM sample preparation by ion milling/amorphization, Micron, 30[3]:267-276, 1999.
21. J. F. Rufner, R. H. R. Castro, T. B. Holland, K. van Benthem, Mechanical properties of individual MgAl2O4 agglomerates and their effects on densification, Acta Materialia, 69[0]:187-195, 2014.
22. F. V. Lenel. Powder metallurgy: principles and applications: Metal Powder Industries Federation, 1980.
23. B. N. Kim, K. Hiraga, K. Morita, Kinetics of normal grain growth depending on the size distribution of small grains, MATERIALS TRANSACTIONS, 44[11]:2239-2244, 2003.
24 S. L. Dole, S. Prochazka, R. H. Doremus, Microstructural Coarsening During Sintering of Boron Carbide, Journal of the American Ceramic Society, 72[6]:958-966, 1989.
25. R. M. German, Sintering theory and practice, Sintering Theory and Practice, by Randall M. German, pp. 568. ISBN 0-471-05786-X. Wiley-VCH, January 1996., 1[1996.
26. Song Y, Dhar S, Feldman LC, Chung G and Williams JR. Modified Deal Grove model for the thermal oxidation of silicon carbide. Journal of Applied Physics 2004;95:4953-4957.
27. Y. Z. Yao, Y. Ishikawa, Y. Sugawara, K. Sato, K. Danno, H. Suzuki, T. Bessho, S. Yamaguchi, K. Nishikawa, Correlation between etch pits formed by molten KOH+Na2O2 etching and dislocation types in heavily doped n(+)-4H-SiC studied by X-ray topography, Journal of Crystal Growth, 364[7-10, 2013.
28. D. Zhuang, J. H. Edgar, Wet etching of GaN, AlN, and SiC: a review, Materials Science and Engineering: R: Reports, 48[1]:1-46, 2005.
29. V. Presser, A. Loges, Y. Hemberger, K. G. Nickel, Microstructural Evolution of Silica on Single-Crystal Silicon Carbide. Part I: Devitrification and Oxidation Rates, Journal of the American Ceramic Society, 92[3]:724-731, 2009.
30. Oshcherin BN. On surface energies of ANB8-N semiconducting compounds. physica status solidi (a) 1976;34:K181-K186.
31. Eustathopoulos N, Nicholas G and Drevet B. Wettability at High Temperatures. 1999.
32. H. Ye, G. Rixecker, F. Aldinger. Liquid Phase Sintered SiC with SiO2 Additive. Ceramics – Processing, Reliability, Tribology and Wear. Wiley-VCH Verlag GmbH & Co. KGaA, 2006. p.172-177.
33 K. Imaizumi, H. Handa, R. Takahashi, E. Saito, H. Fukidome, Y. Enta, Y. Teraoka, A. Yoshigoe, M. Suemitsu, Oxygen-induced reduction of the graphitization temperature of SiC surface, Japanese Journal of Applied Physics, 50[7 PART 1]:2011.
34 W. Kaplan, D. Chatain, P. Wynblatt, W. C. Carter, A review of wetting versus adsorption, complexions, and related phenomena: the rosetta stone of wetting, Journal of Materials Science, 48[17]:5681-5717, 2013.

בתוספת של 0.5% משקלי של בור ו3% משקלי של פחמן למשך 4 שעות הגיעו לצפיפות של כ 96% עם מיקרומבנה המאופיין בגרעינים שווי צירים בעיקרם.

תפקיד הפחמן בחיזור שכבת הסיליקון אוקסיד מפני השטח של סיליקון קרביד הוצג בצורה ישירה על ידי שימוש במודל הניסיוני. במודל ניסוני זה נעשה שימוש במיקרוסקופית אלקטרונים חודרת ברזולוציה גבוהה על מנת לעקב אחרי שלבי החמצון והחיזור של גביש יחיד של סיליקון קרביד. בתהליך זה דגם דק המיועד לשימוש באופן סטנדרטי במיקרוסקופ אלקטרונים חודר, הוכן מפיסת גביש יחיד של סיליקון קרביד, לאחר הכנתו הדגם אופיין והועבר לטיפול תרמי באוויר בטמפרטורה של 1400 מעלות צלזיוס, לאחר אפיון נוסף באמצעות מיקרוסקופ אלקטרונים חודר, על מנת להעריך את גודל שכבת התחמוצת שהתפתח, הדגם כוסה בשכבת פחמן ע"י שימוש במכשיר לנידוף פחמן, ובהמשך הועבר לתהליך חיזור בטמפרטורה של 1400 מעלות צלזיוס בהתאם לידוע מתגובת החיזור של סיליקון אוקסיד ע"י פחמן ומשם לאפיון נוסף. בצורה זו ניתן להראות כי שכבת סיליקון אוקסיד בעובי של כ 30 ננומטר חוזר למעשה בחלק מאזורי הדגם על ידי הפחמן, בדומה למתרחש על גבי פני השטח של גרעיני הסיליקון קרביד בזמן תהליך הסנטור. העדר הציפוף עבור סיליקון קרביד ללא תוספים הוסבר אף הוא כנובע מאנרגית פני השטח הנמוכה של שכבת SiO_2 גם בהשוואה לאנרגיית גבולות הגרעינים הנמוכה ביותר האפשרית בסיליקון, לפיכך קיומה של שכבה זו על פני השטח מקטין את הכוח המניע לציפוף בו מוחלפים פני שטח בגבולות גרעינים, כאשר אנרגיית פני השטח נמוגה מזו של גבולות הגרעינים, לא תהיה ירידה באנרגיה החופשית הכוללת במערכת, והכוח המניע לציפוף לכן דועך.

האופי הקוולנטי של קשר ה Si-C, או כתוצאה מאנרגית גבול גרעין גבוהה, אשר מעקבת את הציפוף דרך פגיעה במנגנוני דיפוזיה או חוסר אינטרינזי בכוח מניע תרמו דינמי לציפוף בסיליקון קרביד.

על מנת להבין בצורה מלאה יותר את מנגנון ההיווצרות של מיקרו מבנה נקבובי וגס זה, יחד עם מאפייני הסנטור של סיליקון קרביד, יש צורך להתייחס לשיקולים ולכוחות המניעים התרמו-דינאמיים המעורבים בתהליך הסנטור, תוך מתן התייחסות לכלל הסוגים של אנרגיות גבולות הגרעין ושל פני השטח הקיימים במערכת.

מטרתו העיקרית של מחקר זה היא השגת הבנה טובה יותר אודות הפיסיקה העומדת מאחורי תהליך הסנטור של סיליקון קרביד, בדגש על סנטור בפאזה מוצקה וללא הפעלתו של לחת חיצוני, וזאת על ידי ניתוח השפעת תוספי הסנטור בור ופחמן, הטמפרטורה וכן הזמן על התפתחות המיקרומבנה. מטרה זו תושג על ידי פיתוחו של תהליך סנטור ללא הפעלת לחץ חיצוני, בסנטור בפאזה מוצקה של סיליקון קרביד, תוך שימוש במגוון רחב ומקיף של שיטות אפיון חומרים, כמיקרוסקופית אלקטרונים חודרת (TEM) מיקרוסקופית אלקטרונים סורקת (SEM) וספקטרוסקופיה של פיזור קרני X בתהליך, וכן על ידי ישומו של מודל ניסיוני אשר יראה בצורה ישירה את תפקיד הפחמן בסנטור של סיליקון קרביד כמחזר SiO_2 מפני השטח של סיליקון קרביד.

במחקר זה פותח על כל שלביו תהליך סנטור מוצלח של קרמיקת סיליקון קרביד, על ידי שימוש בסנטור ללא לחץ חיצוני בפאזה מוצקה ע"י הוספת 0.5% של בור ו 3% משקלי של פחמן. האבקה הגולמית, כפי שהתקבלה מהיצרן, עברה תהליך טחינה בעזרת כדוריות עשויות סיליקון קרביד ובתוספת חומר מרכך אשר נועד למנוע היווצרות תלכידי חלקיקים בתרחיף. לאחר תהליך של יבוש וניפוי האבקה נדחסה ליצירת גופים ירוקים ע"י שימוש בלחיצה חד צירית ולאחר מכן לחיצה איזו סטטית קרה. הגופים הירוקים עברו תהליך של סנטור באווירת הליום בזרימה מתמדת בטמפרטורה של 2100 מעלות צלזיוס למשך זמנים שונים. השפעתם של תוספי הסנטור השונים וכן תנאי הסנטור, טמפרטורה וזמן, נבדקו והוערכו בעזרת מיקרוסקופ אלקטרונים סורק ומיקרוסקופ אלקטרונים חודר, באמצעות ספקטרוסקופיה של פיזור קרני –X ובמדידות צפיפות בשיטת ארכימדס. דגמים אשר עברו סנטור ללא תוספים לא עברו ציפוף והתאפיינו במיקרומבנה נקבובי וגס וכן בנוכחותה של שכבת סיליקון אוקסיד אמורפית. דגמים אשר עברו תהליך סנטור ללא רק אחד מהתוספים פחמן או בור לא עברו ציפוף אף הם והציגו מיקרומבנה גס ונקבובי דומה לזה של דגמים אשר עברו תהליך סנטור ללא תוספים כלל, בדגם אשר עבר תהליך סנטור בתוספת פחמן בלבד הופיעה שכב אמורפית המורכב מפחמן, סיליקון וחמצן. דגמים אשר עברו תהליך סנטור

תקציר

סיליקון קרביד (SiC) הינו חומר קראמי הנמצא בישומים רבים כגון מערכות בלימה מתקדמות לרכבים, מסבי כדורים עמידים, אפודי מגן בליסטים וכן יישומים נוספים הדורשים עמידות גבוהה בשחיקה ובטמפרטורה גבוהה. לסיליקון קרביד ישנם שימושים רבים גם כמוליך למחצה בתעשיית המיקרואלקטרוניקה, כמוליך למחצה בעל פס רחב, עם עמידות גבוהה לטמפרטורה. עבור רוב שימושיו כחומר מבנה נעשה שימוש בחומר רב גבישי עם דרישות לצפיפות גבוהה וכן פרמטרים מכאניים שונים. תהליך הסנטור של סיליקון קרביד נעשה בטמפרטורת גבוהות, מעל 2000 מעלות צלזיוס, באווירה מגנה למניעת חמצון, תוך שימוש בתהליך סנטור בעזרת לחץ כגון לחיצה חד צירית חמה או לחיצה איזו סטאטית חמה, או ללא הפעלת לחץ חיצוני, ובמקביל על ידי תהליך של סנטור בפאזה נוזלית, על ידי הוספת פאזות משניות כגון Al_2O_3 ו Y_2O_3 העוברות התכה בטמפרטורת הסנטור וכך יוצרות כוחות קפילאריים בתוך גוף העובר את תהליך הסנטור וכן מאפשרות מעבר מסה דרך הפאזה הנוזלית, או על ידי שימוש בתהליך סנטור בפאזה מוצקה. לבחירת שיטת הסנטור המסויימת יש השפעה על התכונות המכאניות והפונקציונאליות של החומר המושפעות הן מנוכחות פאזות משניות והן ממאפייני המיקרו – מבנה של החומר.

תהליך סנטור ללא לחץ, בפאזה מוצקה, של סיליקון קרביד היא שיטת הסנטור המועדפת על פי רוב הן מטעמים כלכליים והן על מנת להימנע מנוכחותן של אותן פאזות משניות אשר עלולות להשפיע לרעה על תוכנות המכאניות, ודורשת הוספת תוספי סנטור כאשר לרוב נעשה שימוש בבור ופחמן. תפקידם של בור ופחמן בתהליך הסנטור נחקרו במספר מחקרים בעבר, תפקידו של הפחמן נחשב להיות חיזור של שכבת SiO_2 (סיליקה) מפני השטח של סיליקון קרביד, אשר הודות למנגנון אשר טבעו לא ברור, מונע את פעילותם של מנגנוני העברת מסה בחומר, בנפח ובגבולות הגרעינים, האחראים על קידום הציפוף. תפקידו של בור למעשה לא ידוע ונחשב כאחראי על עיקוב דיפוזיית פני שטח ו\או האצה של דיפוזיית גבולות גרעינים, המונעים תהליך של התגסות והמאיצים את תהליך הציפוף. מכל מקום, עד כה, למיטב ידיעתנו, גישה ישירה להדגמת אף אחד מהמנגנונים לא הודגמה בניסוי, כאשר מרבית המחקרים בתחום נוקטים בגישה עקיפה בה מתבצע אפיון של פרמטרי המיקרו מבנה כדוגמת גודל ונפח נקבוביות. על מנת להבין את תפקידם בתהליך הסנטור של בור ושל פחמן, יש צורך במודל ניסיוני אשר יבודד את המשתנים בסנטור זה מזה ויאפשר לזהות את השפעת התוספים בנפרד.

עבור סנטור ללא לחץ של סיליקון קרביד, ללא שימוש בתוספי סנטור כפחמן ובור, מתקבל מיקרו- מבנה ורמיקולרי נקבובי גס והחומר לא עובר תהליך ציפוף. תופעה זו אשר גם כן נחקרה בעבר, הוסברה כנובעת מתכונה פנימית של החומר כדוגמת

תודות

מחקר זה נעשה בהנחייתו של פרופסור ויין ד. קפלן מהפקולטה למדע והדסה של חומרים בטכניון - מכון טכנולוגי לישראל.

אני מודה לטכניון על התמיכה הכספית הנדיבה בהשתלמותי.

ברצוני להביע תודה לפרופ 'וויין קפלן על העידוד הן ברמה האישית והן ברמה המחקרית , על הקניית שיטות עבודה מקצועיות ,על הדיונים הפוריים וכמובן על דלת פתוחה בכל יום ושעה במשרדו.

השפעת תוספים על סינטור והתפתחות המיקרו-מיבנה ב SiC

חיבור על מחקר

לשם מילוי חלקי של הדרישות לקבלת התואר

מגיסטר למדעים במדע והנדסה של חומרים

ערן גרוס

הוגש לסנט הטכניון – מכון טכנולוגי לישראל

השפעת תוספים על סינטור והתפתחות המיקרו-מיבנה ב SiC

ערן גרוס